



Geochemical constraints on the petrogenesis of granitoids in the East Kunlun Orogenic belt, northern Tibetan Plateau: Implications for continental crust growth through syn-collisional felsic magmatism

Hui Huang ^{a,b,*}, Yaoling Niu ^{a,b,c,*}, Geoff Nowell ^a, Zhidan Zhao ^b, Xuehui Yu ^b, Di-Cheng Zhu ^b, Xuanxue Mo ^b, Shuo Ding ^b

^a Department of Earth Sciences, Durham University, Durham DH1 3LE, UK

^b State Key Laboratory of Geological Processes and Mineral Resources, and School of Earth Science and Mineral Resources, China University of Geosciences, Beijing 100083, China

^c Institute of Oceanology, Chinese Academy of Sciences, Qingdao 266071, China



ARTICLE INFO

Article history:

Received 8 March 2013

Received in revised form 23 December 2013

Accepted 14 January 2014

Available online 24 January 2014

Editor: L. Reisberg

Keywords:

East Kunlun

Enclaves

Cumulate

Syn-collisional granitoids

Crust growth

Paleo-Tethyan

ABSTRACT

Early Triassic syn-collisional granitoids with mafic magmatic enclaves (MMEs) crop out along the entire East Kunlun Orogenic belt (EKOB) at the northern margin of the Tibetan Plateau. They are andesitic in composition and enriched in light rare earth elements (LREEs) with a flat heavy REE (HREE) pattern. Their average composition resembles that of the bulk continental crust. The enclosed MMEs have the same mineralogy as their host granitoids, but contain a greater mode of mafic minerals (amphibole and biotite), and thus have higher HREE abundances. Zircon U-Pb dating shows that both the granitoid hosts and MMEs have the same crystallization age of ~250 Ma and indistinguishable bulk rock Sr-Nd-Pb-Hf isotope compositions (I_{Sr} of 0.7080–0.7116, varying $^{206}\text{Pb}/^{204}\text{Pb}$ of 18.53–19.32, essentially constant $\varepsilon_{\text{Nd}(t)}$ of –5.3 to –2.1 and a small range of positive $\varepsilon_{\text{Hf}(t)}$, mostly 1.7–5.2). The complete isotopic overlapping between the granitoid hosts and the MMEs is understood to reflect that the MMEs are disintegrated cumulates formed at an early stage of the granitoid magma evolution within the same magmatic system. The isotopic data set reveals that the granitoids are variably evolved melts produced by partial melting of the subducted Paleo-Tethyan oceanic crust with terrigenous sediments under amphibolite-facies conditions in response to the continental collision.

© 2014 Elsevier B.V. All rights reserved.

1. Introduction

The origin and evolution of continental crust has been of great interest to geoscientists. Its andesitic bulk composition, arc-like geochemical signature characterized by enrichment in large ion lithophile elements (e.g., Rb, Cs, K, and especially Pb) and depletion in high field strength elements (e.g., Nb, Ta, and Ti) have led to the standard “island arc model” in which continental crust is produced through subduction-zone magmatism (Taylor, 1967, 1977; Taylor and McLennan, 1985; Rudnick and Gao, 2003). In spite of its popularity, this model fails to explain several basic observations (see Niu and O’Hara, 2009; Niu et al., 2013). For example, bulk island arc rocks are basaltic (Arculus, 1981; Gill, 1981; Pearcey et al., 1990) while the bulk continental crust is andesitic (Taylor and McLennan, 1985; Hans Wedepohl, 1995; Rudnick and Gao, 2003; also see Mo et al., 2008); and arc rocks are highly enriched in Sr while bulk continental crust is relatively depleted in Sr (Niu and O’Hara, 2009). Besides, arc crust production and continental destruction

(sediment recycling and subduction-zone erosion) have been demonstrated repeatedly to be mass balanced (von Huene and Scholl, 1991; Clift and Vannucchi, 2004; Clift et al., 2009; Niu and O’Hara, 2009; Scholl and von Huene, 2009), implying that there is no net crustal growth associated with active seafloor subduction and arc magmatism. It has been accepted that the bulk continental crust has grown progressively through episodic magmatism over Earth history (Reymer and Schubert, 1984; Condie, 2000). This notion requires a tectonic setting where juvenile crust is produced and also preserved in order to maintain the net crustal growth (see Niu and O’Hara, 2009; Niu et al., 2013).

A hypothesis that continental collision zones are primary sites of net continental crustal growth was recently proposed by Niu et al. (2007), Mo et al. (2008) and Niu and O’Hara (2009) based on studies of the India-Asia syncollisional (~55 Ma) andesitic rocks from southern Tibet (Mo et al., 2007a, 2008) in order to resolve the major problems that the standard ‘island arc’ model faces (see the above, and reviewed by Niu et al., 2013). These rocks, in particular the syn-collisional andesites, show remarkable compositional similarity to the bulk continental crust (Rudnick and Gao, 2003), yet have strong mantle isotopic signatures (Mo et al., 2007a, 2008). Their petrogenesis is interpreted to represent net mantle-derived materials added to the continents via partial

* Corresponding authors at: Department of Earth Sciences, Durham University, Durham DH1 3LE, UK.

E-mail addresses: hui.huang.geo@gmail.com (H. Huang), yaoling.niu@foxmail.com (Y. Niu).

melting of last fragments of underthrusting Tethyan ocean crust under amphibolite-facies conditions in a syn-collisional setting (Niu and O'Hara, 2009). Nevertheless, whether this hypothesis is valid for older syncollisional granitoids on a global scale still needs testing (Niu et al., 2013).

The Greater Tibetan Plateau is an ideal test ground as it records several continental collision events since the Early Paleozoic (Dewey et al., 1988; Harris et al., 1988a; Yin and Zhang, 1997), as indicated by a number of suture zones with associated syn-collisional granitoid batholiths increasingly younger from the northeast to southwest (Fig. 1A, Harris et al., 1988a). The East Kunlun Orogenic belt (EKOB) in the northern part of the Plateau, which includes abundant syn-collisional granitoids, is one of the largest continental collision zones. It is much older than the India-Asia collision (~250 Ma vs. ~55 Ma). The A'nyemaqen suture zone in the southern EKOB records the closure of the Paleo-Tethyan Ocean and a continental collision event (Yang et al., 1996, 2009). The abundant late Permian to early Triassic granitoids along the EKOB have not been properly studied but only mentioned in regard to subduction/collision related (Harris et al., 1988a; Jiang et al., 1992; Yin and Harrison, 2000) hybrids between mantle-derived melts and crustal materials (Luo et al., 2002; Deng et al., 2004; Chen et al., 2005; Mo et al., 2007b). This interpretation is based on the observations that most EKOB intrusions are I-type granitoids containing mafic magmatic enclaves (MMEs, see definition by Barbarin, 2005) with the latter being considered as representing mantle-derived melts. The same age and overlapping radiogenic isotope compositions between the host granitoids and MMEs are considered as evidence for mixing and "homogenizing" processes (Liu et al., 2004a; Mo et al., 2007b) although it is physically not straightforward how the invoked mixing and "homogenizing" processes only 'homogenized' isotopes without affecting major element compositions.

Here we report major elements, trace elements and bulk-rock Sr-Nd-Pb-Hf isotopes and zircon U-Pb age data on granitoids and MMEs from the EKOB to constrain the petrogenesis of these rocks in the context of understanding the evolution of the EKOB, which also helps understand the evolution of the Paleo-Tethyan system and mechanisms of crust growth in response to continental collision.

2. Geological setting

2.1. Regional and local geology

The EKOB records a complex history of seafloor spreading, subduction and continental collision since the early Paleozoic (Jiang et al., 1992; Yang et al., 1996; Yin and Harrison, 2000). It lies on the northern Tibetan Plateau with the Songpan-Ganzi Basin to the south and Qaidam Basin to the north (Fig. 1A), extending east-west for up to 1500 km with a north-south width of 50–200 km, and can be subdivided into three tectonic zones according to the major faults (northern, middle and southern zones, see Fig. 1B, Jiang et al., 1992; Yang et al., 1996).

2.1.1. Stratigraphy and metamorphic rocks in EKOB

The basement is dominated by Precambrian granitic gneisses with minor Proterozoic granitoids and migmatites. It crops out in all the three zones overlain by early Paleozoic sedimentary rocks (Harris et al., 1988a; Jiang et al., 1992; Yang et al., 1996) and is considered to have been emplaced between 1.8 Ga and 0.9 Ga (Mo et al., 2007b and references therein). The granitic gneiss represented by the Shaliuhe granitic gneiss in the north EKOB has a peak magmatic age of ~920 Ma (Chen et al., 2007c) and a metamorphic age of ~400–500 Ma (Zhang et al., 2003b; Chen et al., 2007c). Whole rock Sr-Nd-Pb and zircon in situ Hf isotope data indicate that its protolith is upper crustal sedimentary rocks of middle Proterozoic age (Harris et al., 1988a; Chen et al., 2007b,c). The late Permian molasses and the angular unconformity between the upper-Permian to lower-Triassic marine strata and lower-

Permian terrestrial strata have been recognized in the Paleozoic-Mesozoic sedimentary cover (Jiang et al., 1992; Zhang et al., 2004; Li et al., 2008), indicating a continental uplift event during that time.

Some ophiolites (Yang et al., 1995, 1996) are exposed along the central Kunlun fault (CKLF) and Kunlun Fault (Fig. 1C), especially in the southern zone, named the A'nyemaqen ophiolite belt. The most precise zircon U-Pb age on these ophiolites within the southern zone is reported for the Dur'ngoi ophiolitic basalt, which is ~308 Ma (Yang et al., 2009).

2.1.2. East Kunlun Batholiths (EK batholiths)

The EKOB contains one of the two largest granitic batholiths on the Greater Tibetan-Plateau (the other being the Gangdese belt in Southern Tibet). The 'Kunlun Batholiths' (Jiang et al., 1992; Mo et al., 2007b) cover 48,400 km², cropping out mostly in the EKOB middle zone (Fig. 1C). The batholiths are mainly monzonite and granodiorite in composition with ages ranging from the Proterozoic to the late Mesozoic (Jiang et al., 1992). The Proterozoic granitoids are part of the Precambrian basement. Early Paleozoic granitoids (400–500 Ma) have been interpreted as resulting from subduction-collision events comparable to that which produced magmatism in the Qilian orogenic belt to the north (Mo et al., 2007b). The granitoids of Late Permian-Early Triassic (P-T) age are dominant in the EKOB with an area of 23,000 km² (Liu et al., 2004a), almost half of the entire batholiths (Mo et al., 2007b). Previous studies indicate that the P-T granitoids are calc-alkaline and formed during the major subduction-related orogenic period (240–260 Ma) (Harris et al., 1988b; Yin and Harrison, 2000; Mo et al., 2007b). Minor mid-late Mesozoic granitoids are also present which might be related to the post-collisional magmatism (Jiang et al., 1992; Mo et al., 2007b). The crystallization ages of P-T granitoids have been determined reliably, yet the origin and petrogenesis of the giant batholiths remains poorly understood. For example, what tectonic setting were they emplaced in during a relatively short time period?

We collected 30 representative samples from 14 locations (GPS data are given in Table 1) around south Dulan and southwest Qinghai Lake (Fig. 1C). The granitoids contain abundant MMEs (Fig. 2A), and thus are ideal to test our hypothesis on the origin of these MMEs in the context of the granitoid petrogenesis. Duplicate samples from some host rocks and MMEs were collected on a meter/centimeter scale in order to look into the potential heterogeneity.

2.2. Petrography

The granitoids are mainly granodioritic in nature with minor granitic and dioritic compositions. They are medium to coarse-grained with equigranular textures. The mineralogy is relatively simple, and is dominated by quartz (Qz, 45–35%), plagioclase (Pl, 35–45%), K-feldspar (Kfs, 5–10%), biotite (Bt, 5%) and minor amphibole (Amp, 2–5%) (Fig. 2C). Accessory minerals include apatite, zircon, and Fe-Ti oxides. The fine grained MMEs are mafic diorite to diorite in composition (Figs. 2D and 3) with oval shapes and varying sizes (Fig. 2A, B). An important observation is that the MMEs have the same mineralogy as the granitoid hosts with higher modes of the mafic minerals such as Amp (30–45%) and Bt (5–10%) (Fig. 2D). No crystal resorption textures and reactive overgrowths have been observed (Fig. 2D).

3. Analytical methods

All the 30 samples (17 granitoid hosts and 13 MMEs including 10 host-MME pairs; Table 1) have been studied. All the analyzed samples were fresh rock chips with weathered surfaces and saw/pen marks removed. They were leached in 5% HCl solution, washed ultrasonically in milli-Q water and dried in a clean environment before being crushed into rock powders (particle size < 50 µm) using agate mills. Major and trace element compositions were analyzed for all the 30 samples

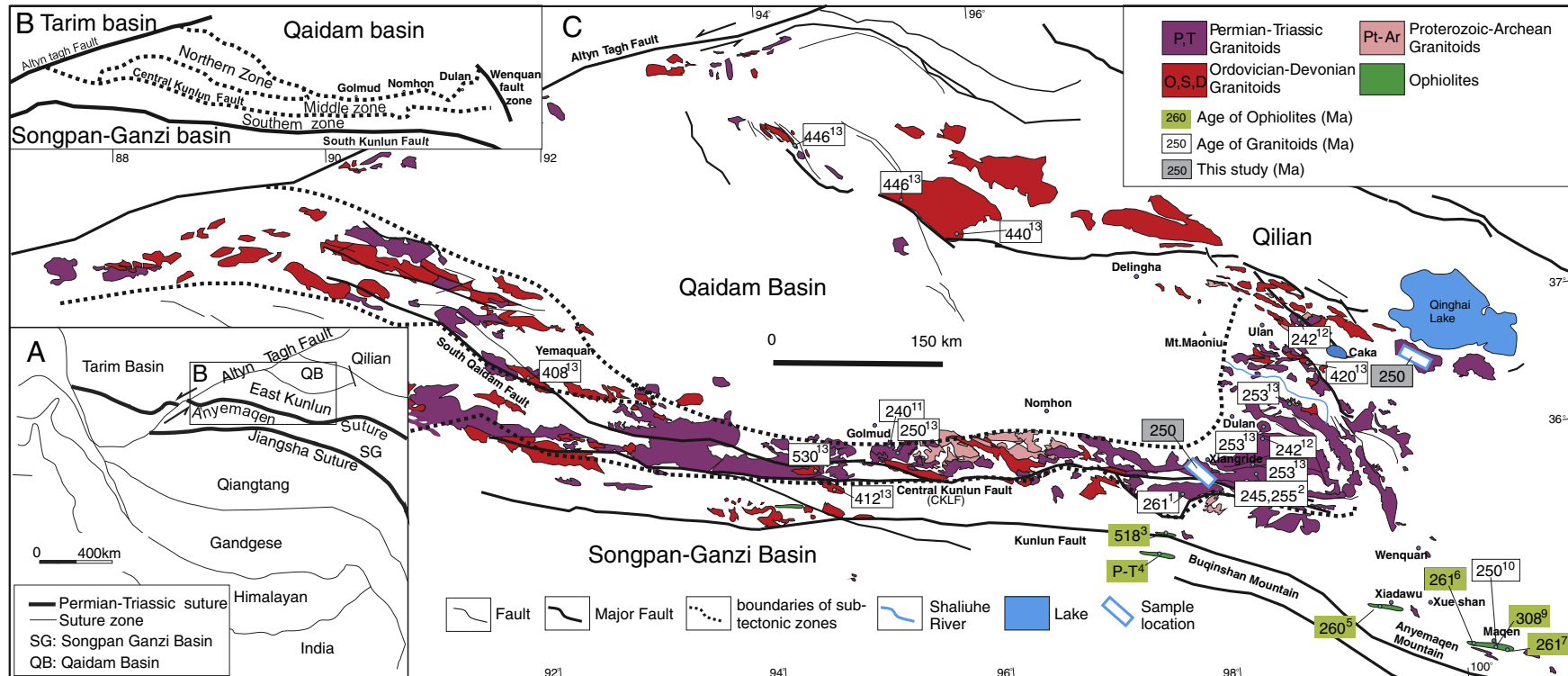


Fig. 1. A, Schematic map showing major tectonic units of West China. B, Schematic map showing three sub-tectonic zones of the East Kunlun Orogenic Belt (EKOB; after Jiang et al., 1992). C, Simplified geological map of the East Kunlun Orogenic Belt and the adjacent Qaidam Basin region showing the distribution of granitoids and ophiolites (after Pan et al., 2004). 1: Naomuhun Pluton, 261 Ma (Xiong et al., 2011). 2: Yuegelu Pluton, 243–256 Ma (Liu et al., 2004b); Halagetu Pluton: 255 Ma (Sun et al., 2009). 3–4 data is from Yang et al. (1996). 3: Qingshuiquan Ophiolite, 518 Ma (Zircon U-Pb). 4: Buqingshan Ophiolite: poorly dated, maybe late Permian to early Triassic. 5: Xiadawu Ophiolite, 260 Ma (Rb-Sr), (Jiang et al., 1992). 6–8 data is from Yang et al. (1996). 6: Majixueshan Ophiolite, Volcanic rocks: 260 Ma (Rb-Sr). 7: Maqen Ophiolite: poorly dated, maybe late Permian to early Triassic. 8: Wanbaogou Ophiolite: poorly dated, maybe late Permian to early Triassic. 9: Dur'ngoi Ophiolite, 308 Ma (Zircon U-Pb) (Yang et al., 2009). 10: Decia granitic complex, 250 Ma (Zircon U-Pb) (Yang et al., 2005). 11: Golmud East, Granodiorite, 240 ± 6 Ma (Zircon U-Pb) (Harris et al., 1988a). 12, Xiangride Pluton, 242 Ma, compilation after Chen et al. (2007b). 13, data from compilation after Chen et al. (2011).

Table 1

Sample location and brief geochemical compositions of EKOB samples.

Sample	GPS position	Type	SiO ₂ %	$\epsilon_{\text{Nd}}(t)$	$\epsilon_{\text{Hf}}(t)$	
DL09-07	N35°45.201'	E98°07.565'	MME	57.9	-2.2	4
DL09-08	N35°45.201'	E98°07.565'	HR	66.8	-3.7	3.3
DL09-09	N35°45.201'	E98°07.565'	HR	68.0	-3.9	-1.3
DL09-10	N35°45.224'	E98°07.563'	HR	67.9		
DL09-11	N35°45.224'	E98°07.564'	MME	57.0		
DL09-12	N35°45.224'	E98°07.564'	HR	71.2		
DL09-13	N35°45.321'	E98°07.669'	HR	65.6	-2.1	2.5
DL09-14	N35°45.321'	E98°07.669'	MME	52.2	-4.5	4.1
DL09-15	N35°47.008'	E98°08.550'	HR	64.9	-3.1	3.5
DL09-16	N35°47.008'	E98°08.550'	MME	50.6	-4.1	5.2
DL09-17	N35°47.008'	E98°08.550'	MME	59.2	-2.2	4.4
DL09-18	N35°47.804'	E98°09.011'	HR	68.9	-2.8	3.4
DL09-19	N35°47.804'	E98°09.011'	MME	54.7		
DL09-20	N35°47.804'	E98°09.011'	MME	58.5		
DL09-21	N35°47.840'	E98°08.991'	HR	66.5	-2.6	2.8
DL09-22	N35°47.840'	E98°08.991'	MME	57.5	-2.9	4.5
DL09-23	N35°48.900'	E98°08.975'	HR	74.2		
DL09-24	N35°48.900'	E98°08.975'	MME	51.9	-4.0	1.8
DL09-25	N35°49.005'	E98°09.004'	HR	64.8		
DL09-26	N35°49.005'	E98°09.004'	MME	48.6	-3.8	4
DL09-27	N35°49.092'	E98°09.401'	HR	67.4	-2.9	2.3
DL09-28	N35°54.088'	E98°01.968'	HR	66.9		
DL09-29	N35°54.107'	E98°01.848'	HR	67.0		
DL09-30	N36°42.712'	E99°33.913'	HR	59.9	-4.9	2.3
DL09-31	N36°42.712'	E99°33.913'	MME	57.7	-5.2	-2.9
DL09-32	N36°42.712'	E99°33.913'	HR	59.3	-5.3	1.7
DL09-33	N36°42.938'	E99°47.356'	HR	65.6		
DL09-34	N36°42.938'	E99°47.356'	MME	57.6		
DL09-35	N36°42.543'	E99°48.067'	HR	66.0		
DL09-36	N36°42.543'	E99°48.067'	MME	57.5		

MME: micro magmatic enclave; HR: Host rock.

(Table 2). Zircons were extracted from 13 samples (including 6 MMEs). Seventeen samples (including 7 MMEs) were analyzed for whole rock Sr–Nd–Pb–Hf isotopic compositions.

3.1. Major and trace elements

Major element analysis was done using XRF (PANalytical Axios Advanced PW4400) on fused glass disks in Tianjin Institute of Geology and Mineral Resources, China following the method of Li et al. (2011). The precision on standards (GSR-1, GSR-3, GSR-8, GSR-9) was better than 3% and mostly better than 0.5%. Trace element analysis was done using ICP-MS (Thermo Scientific X series^{II}) after acid digestion/dissolution in Teflon bombs in Tianjin Institute of Geology and Mineral Resources, China. Sample preparation information is provided in Appendix A. Standard data are given in Appendix B.

3.2. Bulk-rock Sr, Nd, Pb and Hf isotopes

Bulk-rock Sr, Nd, Pb and Hf isotope analyses were conducted on a Thermo Finnigan Neptune Plasma Ionization Multi-collector Mass Spectrometer (PIMMS) instrument in the Northern Centre for Isotopic and Elemental Tracing (NCIET) at Durham University. The powders were dissolved with HF–HNO₃ mixtures. Sr, Pb and Nd–Hf fractions were separated by small Sr Spec resin columns to obtain Sr and Pb fractions and Nd–Hf bearing fractions. The Nd–Hf fraction was then separated using Hf–Nd AG50W-X8 cation exchange resin columns to obtain purified Nd and Hf fractions. The Hf fraction was further purified through Hf–Ti AG1-X8 anion exchange resin columns to remove any remaining Ti. After the chromatography, the Sr, Nd, Pb and Hf fractions were dried and taken up in 3% HNO₃ for analysis. The mass corrections follow the procedure of Nowell and Parrish (2001) and are summarized in Appendix A. Sr–Nd–Pb–Hf isotopic analyses were carried out during different analytical sessions for each isotope. The international standards NBS987, J&M,

NBS981 and JMC475 were used for Sr, Nd, Pb and Hf isotopes, respectively. The long term performance of the Neptune PIMMS at Durham University for Sr, Nd and Hf isotopes was reported by Nowell et al. (2003). Details relating to standard normalization, precisions and total chemistry blanks are given in Tables 3–6. Details of preparation methods, chemical separation techniques and instrument running conditions are given in Appendix A.

3.3. Zircon U–Pb dating

About 100–150 zircon grains for each of the studied samples were mounted in an epoxy resin disk and then grinded/polished to expose the zircon interiors for imaging and analysis. All the polished zircon grains were photographed under transmitted- and reflected-light, and further examined using cathodoluminescence (CL) images prior to the U–Pb analyses. Laser ablation ICP-MS zircon U–Pb analysis was carried on an Agilent 7500 ICP-MS instrument equipped with a GeoLas 2005 at China University of Geosciences, Wuhan. Detailed operating conditions for the laser ablation system and ICP-MS instrument and data reduction are the same as described by Liu et al. (2008). Zircon 91500 was used as the external standard and ran twice every 5 samples. Standard silicate glass NIST610 was used to optimize the instrument. Beam diameter was 30 μm. Common Pb was corrected by ComPbCorr#3_17 (Andersen, 2002). Age calculations and Concordia plots were made using isoplott (Ludwig, 2003).

4. Analytical results

4.1. Major and trace elements

Host granitoids are more siliceous than the contained MMEs (Fig. 3). All of them are calc-alkaline (Fig. 3) and metaluminous ($A/\text{CNK} < 1.1$, Table 2). Three MME samples chemically fall into the gabbro field (Fig. 3), but they are Amp-rich mafic-diorites with no pyroxene present.

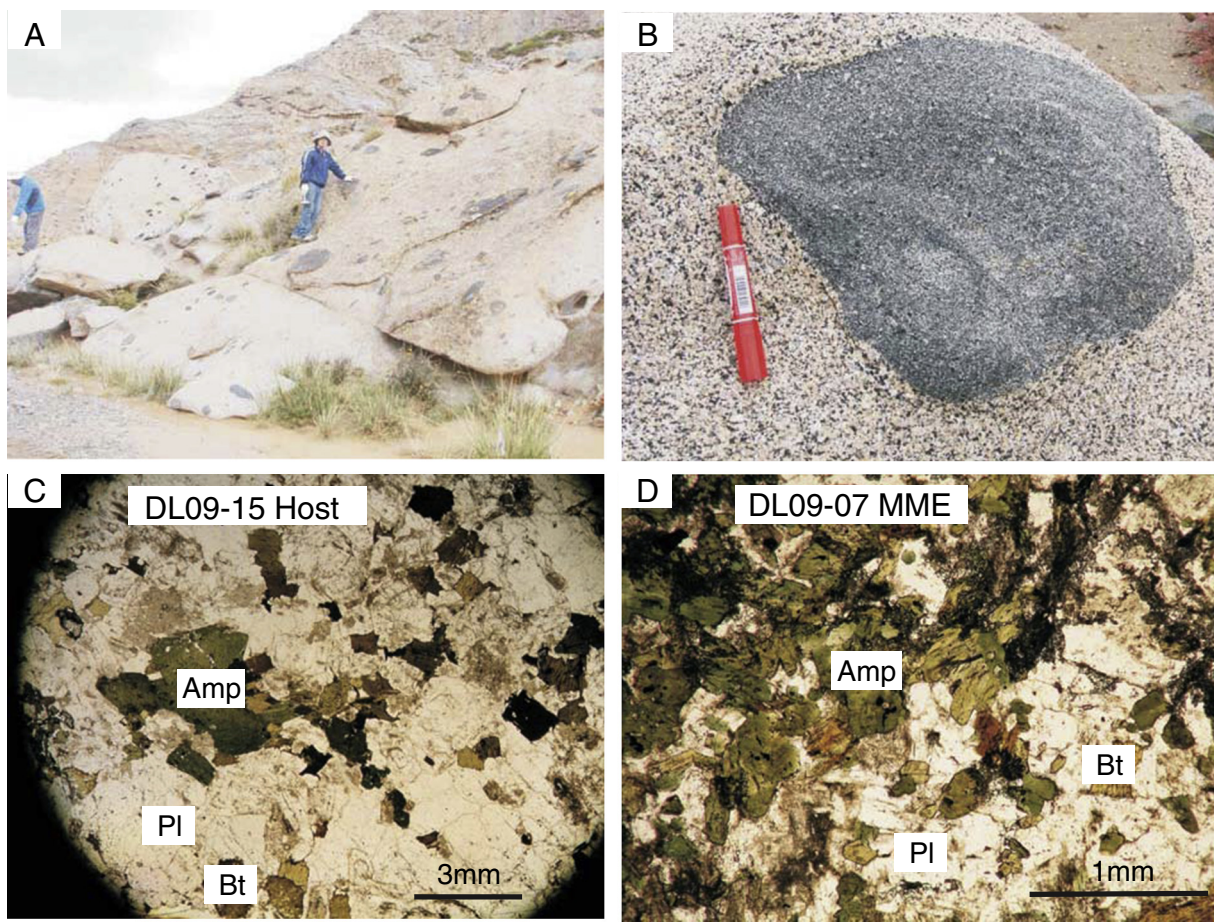


Fig. 2. Field photos in the Dulan area (A–B) and photomicrographs under plane polarized light of the representative granitoid host (C) and enclave (MME) (D).

Host rocks and MMEs define good linear trends for most elements on Harker diagrams (Fig. 4). TiO_2 , Al_2O_3 , FeO , MnO , MgO , CaO , Eu and Yb exhibit well defined negative trends, which likely reflect the fractionation of Amp, Bt and Pl.

Both MMEs and granitoid hosts have an enriched LREE and flat HREE profile lacking a garnet signature (no depletion of HREEs) (Fig. 5A, B).

The average compositions of the granitoid hosts display apparent similarity to the bulk continental crust (BCC) composition in terms of all the analyzed elements and key elemental ratios (Fig. 5C, D) except for the lower Cr, Co, Ni, Sc and Mg in granitoids from the EKOB (Fig. 5C). The lower concentrations of Ni, Cr and Mg relative to the calculated modal BCC composition are typical for normal andesites (vs. high Mg andesites) and fully discussed by Niu and co-authors (Mo et al., 2008; Niu and O'Hara, 2009; Niu et al., 2013). The slightly higher Th/U in the hosts compared to BCC (Fig. 5D) may be inherited from the Paleo-Tethyan MORB (see below) as it has a distinctly higher $^{208}\text{Pb}/^{204}\text{Pb}$ at a given $^{206}\text{Pb}/^{204}\text{Pb}$ compared to other MORB (Xu et al., 2002). MMEs display higher abundances of HREEs (Fig. 5A), reflecting their greater proportions of mafic minerals (e.g., Amp and Bt). The Nb/Ta ratios are all sub-chondritic (chondritic value of 17.5, Sun and McDonough, 1989), 11.84 for host rocks and 13.07 for enclaves. The slightly higher Nb/Ta ratios for enclaves are consistent with higher modal Amp which has super-chondritic Nb/Ta ratios (Foley et al., 2000) as elaborated by Niu and O'Hara (2009). The Sr/Sr^* ($\text{Sr/Sr}^* = 2 \times \text{Sr}_{\text{N}} / [\text{Pr}_{\text{N}} + \text{Nd}_{\text{N}}]$) and Eu/Eu^* ($\text{Eu/Eu}^* = 2 \times \text{Eu}_{\text{PM}} / [\text{Sm}_{\text{PM}} + \text{Gd}_{\text{PM}}]$) for host rocks are 0.78 and 0.84, respectively. The MMEs have slightly lower Sr/Sr^* (0.48) and Eu/Eu^* (0.67) due to a lesser amount of plagioclase. It is important to note that the sub-chondritic Nb/Ta ratios, Nb-Ta-Ti depletion and slight Sr-Eu depletions of these samples are identical to those of the BCC (Fig. 5D) (also see Niu and O'Hara, 2009).

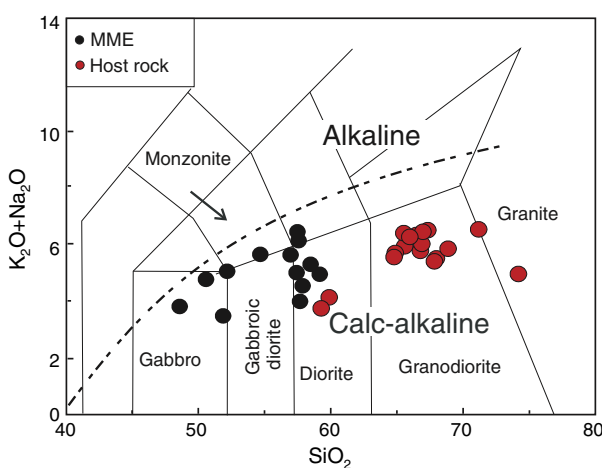


Fig. 3. Total alkalies ($\text{Na}_2\text{O} + \text{K}_2\text{O}$) versus SiO_2 (TAS) diagram showing the compositional variation of EKOB samples. The MMEs are generally less felsic than the hosts. Three samples in the gabbro field are actually mafic-diorite without pyroxene. All the samples are calc-alkaline. The dashed line represents the division between Alkaline and Cal-alkaline fields (Irvine and Baragar, 1971).

4.2. Zircon U–Pb Geochronology

Zircons from host rocks are on average ~100–200 μm long, colorless and euhedral with good prisms and pyramid faces, and have

small elongation ratio of 1:1 to 3:1. They are either uniform or have oscillatory zoning (Fig. 6). Some of them have inherited cores with magmatic overgrowth rims. The Th/U ratios are mostly within the range of 0.4–0.6. A few old inherited zircons with Th/U < 0.1 (Appendix C) have discordant ages (Fig. 7). Zircons from MMEs are brown in color, show cracks under transmitted and reflected light, and are characterized by high length/width ratios and straight rhythmic stripes (Fig. 6). Most zircons yield concordant or slightly discordant U–Pb ages. Zircon U–Pb ages of 7 granitoid hosts indicate that the intrusions were emplaced principally in the late Permian and early Triassic ~250 Ma (Fig. 7). All the 6 MMEs have an identical age to host rocks within error, i.e. ~250 Ma (Fig. 7). Inherited zircon cores which occur in both MMEs and host rocks, plot along or close to the Concordia, yielding age populations around 400–500 Ma and 800–1000 Ma (Figs. 6, 7). These are identical respectively to the metamorphic and magmatic ages recorded in the Shaliuhe gneiss in the region (Zhang et al., 2003a; Meng et al., 2005b; Chen et al., 2007c).

4.3. Whole rock Sr–Nd–Pb–Hf isotopes

Whole rock Sr–Nd–Pb–Hf isotope data for 17 samples (including 7 MMEs) are given in Tables 3–6 and plotted in Figs. 8–11. Contributions from mature continental crust are apparent as I_{Sr} and $Pb_{(i)}$ are radiogenic and all the $\varepsilon_{Nd}(t)$ values are slightly enriched (−5.3 to −2.1 for host rocks and −5.2 to −2.2 for MMEs). I_{Sr} , $Pb_{(i)}$, $\varepsilon_{Nd}(t)$ and $\varepsilon_{Hf}(t)$ refer to the age corrected values and ε_{Nd} and ε_{Hf} refer to the present-day values.

Theoretically, Hf and Nd isotopes are expected to correlate with each other (thus explaining the mantle array, Chauvel et al., 2008) because of the similar behavior of Lu–Hf and Sm–Nd systems during magmatism. However, it has been found that ‘Nd’ and ‘Hf’ can isotopically decouple in some circumstances (Bizimis et al., 2004; Schmitz et al., 2004; Hoffmann et al., 2011). In our study, the majority of $\varepsilon_{Hf(t)}$ values are positive (Table 5) indicating a significant mantle input, which is apparently inconsistent with the suggestion of negative $\varepsilon_{Nd(t)}$. Note that there are broad Lu/Hf vs. $^{176}\text{Hf}/^{177}\text{Hf}$ and Rb/Sr vs. $^{87}\text{Sr}/^{86}\text{Sr}$ correlations, but no

Table 2
Major and trace element data for granitoid hosts and MMEs.

Sample	DL09-07	DL09-08	DL09-09	DL09-10	DL09-11	DL09-12	DL09-13	DL09-14	DL09-15	DL09-016	DL09-017	DL09-018	DL09-019	DL09-020
Pairs	1 MME	1 HR	1 HR	2 HR	2 MME	3 HR	3 MME	4 HR	4 MME	4 MME	4 HR			
SiO ₂	57.9	66.8	68.0	67.9	57.0	71.2	65.6	52.2	64.9	50.6	59.2	68.9	54.7	58.5
TiO ₂	0.66	0.54	0.36	0.46	1.08	0.22	0.54	0.81	0.58	0.78	0.97	0.47	0.90	0.88
Al ₂ O ₃	16.5	15.3	15.9	15.3	16.6	14.8	15.7	17.3	15.8	17.3	14.1	14.7	16.8	16.6
Fe ₂ O ₃	1.74	1.38	1.04	1.78	2.77	0.88	1.90	3.60	1.65	3.36	3.30	1.33	2.68	2.68
FeO	4.70	3.02	3.07	2.18	6.10	1.92	2.62	6.55	3.28	7.20	5.75	2.57	7.10	5.00
MnO	0.14	0.09	0.12	0.10	0.17	0.08	0.09	0.25	0.09	0.27	0.18	0.08	0.25	0.18
MgO	4.46	1.72	0.78	1.42	3.12	0.48	1.69	4.18	2.00	4.75	3.87	1.39	3.89	3.01
CaO	7.51	4.18	4.09	3.95	5.57	2.78	4.31	7.85	4.56	8.81	5.46	3.55	6.07	5.50
Na ₂ O	3.27	3.28	3.41	3.58	3.36	3.27	3.28	3.52	3.24	3.35	2.62	3.30	3.49	3.75
K ₂ O	1.27	2.49	2.10	1.82	2.27	3.26	2.65	1.53	2.46	1.42	2.33	2.55	2.16	1.55
P ₂ O ₅	0.09	0.10	0.14	0.09	0.20	0.08	0.11	0.11	0.11	0.09	0.20	0.10	0.09	0.13
LOI	1.00	0.61	0.59	1.03	0.88	0.78	1.00	1.09	0.68	1.13	1.21	0.68	0.91	1.50
Total	99.51	99.24	99.60	99.56	99.12	99.76	99.49	98.99	99.35	99.06	99.19	99.62	99.04	99.28
A/CNK	0.81	0.97	1.04	1.02	0.92	1.06	0.97	0.80	0.97	0.75	0.84	1.00	0.88	0.93
Li	19.3	25.3	26.1	20.1	31.7	24.1	24.5	25.2	22.5	17.1	29.1	28.9	45.9	38.1
Sc	19.8	9.24	3.40	7.47	22.6	2.85	9.64	23.1	12.3	25.3	32.6	7.95	28.3	22.7
Cr	39.9	7.31	1.56	6.26	9.37	2.27	7.39	46.5	8.25	9.61	15.2	5.59	15.1	11.9
Co	19.6	8.91	3.59	7.44	18.7	2.15	8.99	19.7	10.7	21.6	19.6	7.40	19.2	15.1
Ni	5.38	2.70	0.98	2.39	4.78	0.84	2.70	8.35	2.96	6.31	5.34	2.34	6.61	2.59
Ga	15.1	16.1	19.5	16.3	19.4	17.4	16.3	19.4	16.8	19.2	18.2	15.8	20.5	18.4
Rb	50.6	81.7	81.3	63.9	88.0	106	77.0	73.7	77.4	64.1	101	74.2	123	49.5
Sr	232	172	367	192	177	322	186	197	204	212	169	177	159	177
Y	16.5	17.6	16.8	22.2	33.3	15.6	17.2	50.9	20.1	46.9	45.5	18.3	57.7	33.1
Zr	102	145	215	111	164	171	147	90	155	101	276	157	103	106
Nb	5.24	8.92	12.0	8.29	13.1	11.1	8.2	12.1	8.24	10.0	13.6	8.47	14.6	10.5
Ba	293	459	691	427	567	1030	587	313	523	215	555	554	395	301
La	17.7	12.9	35.5	9.81	32.6	33.1	29.3	15.2	23.9	13.6	27.6	31.8	10.6	9.0
Ce	33.6	23.0	66.4	16.1	64.6	61.5	45.6	45.1	40.1	43.8	62.2	53.2	31.9	23.6
Pr	3.63	3.17	7.37	2.44	8.17	6.80	5.27	7.60	4.89	7.18	8.49	6.18	5.98	4.24
Nd	13.1	12.7	25.7	9.93	31.6	24.0	18.1	34.6	18.0	32.4	35.2	21.1	29.4	19.6
Sm	2.76	2.88	4.16	2.58	6.30	4.07	3.25	8.25	3.60	7.57	7.94	3.64	8.22	4.87
Eu	1.03	0.84	1.25	0.77	1.33	1.16	0.94	1.61	0.97	1.77	1.32	0.86	1.20	1.04
Gd	2.76	2.75	3.52	2.69	5.80	3.34	3.14	7.38	3.41	6.73	7.48	3.36	7.55	4.58
Tb	0.47	0.47	0.52	0.52	1.00	0.50	0.50	1.38	0.57	1.26	1.33	0.53	1.52	0.87
Dy	2.99	3.06	2.94	3.54	6.09	2.89	3.03	8.96	3.58	8.08	8.39	3.18	9.83	5.61
Ho	0.65	0.66	0.62	0.78	1.31	0.59	0.65	1.92	0.75	1.73	1.76	0.68	2.13	1.22
Er	1.81	1.94	1.80	2.32	3.63	1.70	1.87	5.63	2.20	5.12	4.90	1.98	6.26	3.62
Tm	0.28	0.31	0.28	0.40	0.55	0.26	0.29	0.89	0.34	0.82	0.74	0.31	0.99	0.57
Yb	1.89	2.16	1.95	2.68	3.67	1.80	1.99	6.04	2.24	5.61	4.91	2.07	6.72	3.86
Lu	0.29	0.34	0.32	0.42	0.59	0.29	0.32	0.95	0.36	0.90	0.78	0.33	1.04	0.62
Hf	2.89	4.27	5.39	3.37	4.56	4.82	4.12	3.09	4.36	3.25	7.54	4.40	3.34	3.11
Ta	0.48	1.02	0.74	0.84	0.88	0.79	0.78	0.94	0.75	0.64	1.04	0.70	1.11	0.76
Pb	11.5	16.1	14.3	13.0	13.0	24.1	18.7	15.5	15.6	12.7	12.3	17.2	14.7	13.1
Th	4.07	10.2	11.7	3.6	11.1	11.9	11.6	1.73	9.11	2.11	10.6	13.8	3.33	2.47
U	0.74	1.38	1.10	0.85	0.73	1.40	1.26	0.62	1.01	0.60	1.34	1.07	0.89	0.80
Nb/Ta	11.0	8.7	16.2	9.87	14.9	14.1	10.4	12.9	11.1	15.6	13.0	12.1	13.2	13.8
Eu/Eu*	1.13	0.90	0.97	0.89	0.66	0.93	0.88	0.62	0.84	0.74	0.52	0.74	0.46	0.67
Sr/Sr*	0.96	0.78	0.76	1.12	0.32	0.72	0.54	0.35	0.62	0.40	0.28	0.44	0.35	0.56

Sm/Nd vs. $^{143}\text{Nd}/^{144}\text{Nd}$ correlation. This observation, combined with the decoupling between ε_{Nd} and ε_{Hf} could put Nd isotopic data quality into question. For this reason, we have randomly reanalyzed 5 samples for Nd isotopes and the reproducibility is good (<66 ppm; Appendix D). The apparent non-correlation between Sm/Nd and $^{143}\text{Nd}/^{144}\text{Nd}$ can be explained by the small range in $^{147}\text{Sm}/^{144}\text{Nd}$ ratios among our samples and the long half-life of ^{147}Sm , which taken together prevent a statistically significant isochron developing in 250 Ma (Fig. 8C). On the contrary, the large Lu/Hf variation of up to 500% and the short half-life of ^{176}Lu explain the significant Lu/Hf pseudochron.

Nevertheless, it is necessary to consider the potential effect of incomplete digestion of zircons in these samples. For example, our Teflon beaker digestion method for isotope analysis cannot digest zircons completely for the zircon-rich granitoid rocks we study. This can cause problems as $>95\%$ Zr (see partition coefficients of Zr; Fujimaki, 1986) resides in zircons in zircon rich granitoids. If no zircons were dissolved during digestion and assuming

all the Hf resides in zircons, the analyzed Hf must then be Lu decaying product in the non-zircon phases only (Fig. 8). However, this is unlikely to be the case for two reasons: firstly, the digestion using Teflon beakers is able to dissolve zircons to some extent, and thus the Hf hosted in the dissolved portions of zircons will enter the solution accordingly; secondly and importantly, the average size of zircons in the studied samples is 100–200 μm (Fig. 6), yet the rock powder particle size is $\leq 50 \mu\text{m}$ (mostly $<5 \mu\text{m}$), i.e., the zircon fragments of $\leq 50 \mu\text{m}$ size in the solution must be well-exposed with enhanced surface areas, facilitating acid dissolution and digestion. This means that even if zircons may not be completely digested using our Hf-isotope procedure, significant portion of zircons must be digested and analyzed, with the obtained $^{176}\text{Hf}/^{177}\text{Hf}$ ratios likely approaching the bulk-rock ratios. This is demonstrated by the Lu/Hf pseudochron (Fig. 8B), where the $^{176}\text{Lu}/^{177}\text{Hf}$ ratio was obtained through ICP-MS trace element analysis of complete sample digestion (see above).

DL09-021	DL09-022	DL09-023	DL09-024	DL09-025	DL09-026	DL09-027	DL09-028	DL09-029	DL09-030	DL09-031	DL09-032	DL09-033	DL09-034	DL09-035	DL09-036
5	5	6	6	7	7	—	—	8	8	8	8	9	9	10	10
HR	MME	HR	MME	HR	MME	HR	HR	HR	MME	HR	HR	HR	MME	HR	MME
66.5	57.5	74.2	51.9	64.8	48.6	67.4	66.9	67.0	59.90	57.70	59.30	65.55	57.60	66.00	57.50
0.48	0.89	0.20	0.96	0.58	1.39	0.38	0.57	0.53	0.51	0.67	0.58	0.52	0.63	0.48	0.76
15.7	16.7	14.4	18.5	15.9	18.4	16.6	15.9	15.9	17.60	17.30	17.50	15.65	16.40	15.70	15.50
1.55	2.84	0.50	2.48	1.63	3.33	1.36	1.34	1.50	1.72	1.89	1.39	1.17	1.64	1.32	1.42
2.60	4.92	1.06	6.05	3.30	6.65	2.02	2.27	1.70	3.33	4.33	4.03	3.06	5.15	2.57	5.40
0.09	0.18	0.02	0.17	0.09	0.17	0.10	0.06	0.05	0.09	0.12	0.11	0.08	0.15	0.07	0.15
1.46	3.40	0.60	4.57	1.97	5.48	0.98	1.58	1.30	3.50	3.59	3.99	2.02	3.80	1.82	4.29
3.79	6.70	3.36	9.45	4.72	9.10	3.74	3.64	3.70	6.15	7.06	6.78	4.47	6.74	4.53	6.95
3.60	3.46	4.31	2.35	3.21	2.34	4.04	3.95	3.95	2.75	2.34	2.66	3.00	3.09	3.07	2.81
2.73	1.54	0.65	1.13	2.34	1.47	2.46	2.07	2.50	1.38	1.65	1.08	3.40	3.04	3.20	3.64
0.10	0.12	0.05	0.12	0.11	0.12	0.11	0.16	0.14	0.09	0.10	0.10	0.10	0.10	0.09	0.15
0.96	1.14	0.45	1.44	0.78	2.00	0.50	1.17	1.27	2.40	2.53	1.92	0.44	0.78	0.60	0.63
99.56	99.29	99.75	99.12	99.43	99.05	99.59	99.61	99.54	99.42	99.28	99.44	99.46	99.12	99.45	99.20
0.99	0.85	1.03	0.83	0.97	0.84	1.03	1.03	1.00	1.02	0.94	0.98	0.93	0.79	0.94	0.73
29.2	30.4	0.56	19.7	23.5	17.0	22.5	29.4	26.6	22.7	22.2	22.0	51.8	44.8	38.8	44.8
10.4	26.4	1.96	32.6	11.2	32.6	5.42	5.28	4.55	13.9	21.3	16.4	11.2	24.6	9.65	18.6
5.63	24.9	1.73	23.4	8.90	49.9	3.24	8.41	7.93	47.2	19.4	55.4	25.2	14.1	21.1	95.6
7.54	17.6	3.02	21.3	10.8	28.5	5.09	6.90	6.60	11.9	13.2	13.1	10.9	18.8	10.1	19.4
2.30	4.14	1.58	2.99	3.44	12.17	1.91	4.64	4.39	11.8	3.13	11.42	7.09	7.76	6.31	23.7
17.0	17.9	12.0	18.7	16.2	18.6	16.4	20.0	19.6	17.5	17.8	17.6	16.6	18.1	16.2	17.0
88.0	58.3	38.2	50.0	65.5	60.6	54.4	44.5	47.9	43.3	38.2	39.4	154	160	114	179
186	208	154	246	197	279	213	466	502	348	270	347	223	192	213	195
23.8	29.9	14.5	26.1	17.0	30.4	12.4	10.7	9.13	15.5	20.5	18.2	21.0	34.2	18.9	17.5
154	77.1	123	99.4	134	84.8	153	181	166	111	129	116	184	74.3	177	126
9.02	8.25	6.91	6.29	7.61	6.74	9.19	9.84	9.15	7.28	7.75	7.75	10.8	14.1	9.64	11.8
607	392	168	224	564	310	698	688	867	288	314	238	424	408	427	508
29.6	17.9	10.0	13.3	20.2	16.8	18.9	28.6	31.4	17.3	21.2	20.2	27.6	24.6	22.6	28.3
51.5	46.8	21.6	34.5	32.4	34.9	32.4	52.3	56.2	34.4	42.5	42.2	52.0	58.5	42.6	50.9
6.06	6.29	2.24	4.88	4.17	4.47	3.76	6.38	6.43	4.23	5.13	4.91	6.15	7.85	5.24	5.61
21.7	24.9	8.4	20.0	15.6	18.7	13.4	23.5	22.5	16.0	19.5	18.7	22.0	30.2	19.5	19.9
4.22	4.87	1.79	4.42	3.10	4.60	2.51	3.96	3.66	3.14	3.91	3.73	4.09	6.34	3.73	3.76
0.95	1.16	0.61	1.26	0.90	1.38	0.97	1.01	0.96	0.76	0.97	0.84	0.84	0.83	0.86	0.80
3.85	4.50	1.78	4.20	2.95	4.76	2.37	3.15	2.92	2.82	3.56	3.28	3.61	5.61	3.31	3.40
0.66	0.78	0.33	0.74	0.48	0.88	0.36	0.43	0.37	0.47	0.62	0.55	0.60	0.98	0.54	0.54
4.15	5.09	2.20	4.78	3.01	5.63	2.18	2.19	1.86	2.81	3.80	3.35	3.69	6.08	3.30	3.29
0.90	1.10	0.50	1.03	0.64	1.21	0.45	0.39	0.34	0.60	0.78	0.70	0.77	1.26	0.71	0.68
2.59	3.26	1.53	2.86	1.79	3.36	1.33	1.04	0.91	1.68	2.22	1.94	2.24	3.65	2.07	1.92
0.41	0.52	0.25	0.43	0.28	0.51	0.20	0.15	0.12	0.26	0.33	0.30	0.35	0.57	0.31	0.29
2.76	3.62	1.82	2.79	1.90	3.17	1.38	0.99	0.80	1.68	2.22	1.95	2.36	3.86	2.12	2.03
0.45	0.57	0.30	0.44	0.30	0.49	0.23	0.14	0.12	0.27	0.35	0.31	0.37	0.61	0.33	0.34
4.45	2.28	3.71	2.96	3.73	2.57	4.09	4.78	4.41	3.20	3.53	3.36	5.14	2.72	4.87	3.46
0.88	0.53	0.67	0.52	0.63	0.49	0.60	0.73	0.68	0.63	0.58	0.63	1.17	1.52	0.93	1.03
19.4	10.8	13.8	7.0	13.8	6.47	13.77	8.17	9.07	9.79	7.52	10.4	17.2	16.7	15.8	15.6
14.1	3.39	7.40	5.29	7.72	3.84	7.10	10.8	8.96	6.94	7.39	7.25	17.5	11.6	13.4	12.9
1.95	0.67	1.76	1.23	1.21	1.25	0.77	1.80	1.65	0.83	1.30	0.98	0.93	0.87	0.67	1.20
10.2	15.5	10.3	12.1	12.0	13.7	15.4	13.5	13.4	11.6	13.4	12.3	9.22	9.29	10.4	11.4
0.71	0.74	1.04	0.88	0.90	0.90	1.19	0.84	0.87	0.76	0.78	0.72	0.66	0.42	0.73	0.67
0.46	0.48	1.01	0.71	0.70	0.88	0.86	1.09	1.19	1.21	0.77	1.04	0.55	0.36	0.60	0.53

Table 3

Whole rock Sr isotopic data. The last column refers to the analytical session during which the sample was analyzed for Sr isotope composition. The blank, the average $^{87}\text{Sr}/^{86}\text{Sr}$ and reproducibility of multiple measurements of the NBS987 Sr isotope standard during the appropriate session are given below:

- 1: 0.710267 ± 0.01 (2SD, n = 13), blank = 8 pg
- 2: 0.710283 ± 0.02 (2SD, n = 8), blank = 23 pg
- 3: 0.710284 ± 0.05 (2SD, n = 9), blank = 24 pg.

$^{87}\text{Sr}/^{86}\text{Sr}$ are reported relative to an accepted $^{87}\text{Sr}/^{86}\text{Sr}$ ratio for NBS987 of 0.71024 (Thirlwall, 1991).

Sample	Type	Rb (ppm)	Sr (ppm)	$^{87}\text{Rb}/^{86}\text{Sr}$	$^{87}\text{Sr}/^{86}\text{Sr}$ (2SD)	I_{sr}	Analytical sessions
DL09-07	MME	50.6	232	0.62	0.711636 (12)	0.70944	1
DL09-08	HR	81.7	172	1.35	0.714290 (10)	0.70950	1
DL09-09	HR	81.3	367	0.63	0.713877 (13)	0.71164	1
DL09-13	HR	77.0	186	1.17	0.713729 (20)	0.70956	1
DL09-14	MME	74.0	197	1.06	0.713029 (12)	0.70925	2
DL09-15	HR	77.4	204	1.07	0.713498 (11)	0.70968	1
DL09-16	MME	64.0	212	0.86	0.712413 (11)	0.70937	2
DL09-17	MME	101	169	1.69	0.715355 (13)	0.70933	1
DL09-18	HR	74.2	177	1.18	0.714678 (13)	0.71046	1
DL09-21	HR	88.0	186	1.34	0.714763 (09)	0.70999	1
DL09-22	MME	58.3	208	0.79	0.712593 (12)	0.70977	1
DL09-24	HR	50.0	246	0.58	0.712486 (07)	0.71044	3
DL09-26	MME	60.6	279	0.62	0.711845 (11)	0.70966	2
DL09-27	HR	54.4	213	0.72	0.712073 (12)	0.70950	1
DL09-30	HR	43.3	348	0.35	0.709680 (09)	0.70843	1
DL09-31	MME	38.2	270	0.40	0.709370 (12)	0.70795	1
DL09-32	HR	39.4	347	0.32	0.709288 (11)	0.70814	1

$$I_{\text{sr}} = (\frac{^{87}\text{Sr}}{^{86}\text{Sr}})_{\text{sample}} - (\frac{^{87}\text{Rb}}{^{86}\text{Sr}})_{\text{sample}} * (e^{\lambda t} - 1), \lambda(^{87}\text{Rb}) = 1.42 \times 10^{-11} \text{ yr}^{-1}.$$

Therefore, the apparent decoupling of Nd isotope with Hf (and Sr) isotopes is significant, and the age-corrected initial Hf–Nd–Sr isotopic ratios can be reliably used to trace magma sources and processes.

5. Discussion

5.1. Isotope constraints on the formation of MMEs

I-type granitoids usually contain various amounts of MMEs (Holden et al., 1987; Winter, 2010). The origin of the MMEs can hold clues to the petrogenesis of the entire granitoid–MME systems, yet the origin remains debated. For example, MMEs have been interpreted as restites (Chappell et al., 1987, 1999); as representing mantle derived melts

(Barbarin, 2005; Mo et al., 2007b; Yang et al., 2007; Clemens and Stevens, 2011); or as mafic cumulate (Wall et al., 1987; Dahlquist, 2002; Niu et al., 2013). In the case of the EKOB, MMEs were interpreted to represent mantle melts involved in magma mixing because of their mafic composition. Nevertheless, their negative $\varepsilon_{\text{Nd}(t)}$ and relatively radiogenic Sr and Pb isotopes (Liu et al., 2004b; Chen et al., 2011; Xiong et al., 2011) are indistinguishable from those of the host rocks, arguing that if they are indeed mantle melts, they must be derived from an unusually enriched mantle source (Liu et al., 2004b; Xiong et al., 2011).

It is not always straight forward to distinguish a cumulate process from a mixing process in terms of major and trace element data because both techniques can produce linear trends on Harker plots (Clemens and Stevens, 2011). In this case, isotopes are robust tools

Table 4

Whole rock Nd isotopic data. The last column refers to the analytical session during which the sample was analyzed for Nd isotope composition. The blank and average $^{143}\text{Nd}/^{144}\text{Nd}$ and reproducibility of multiple measurements of the J&M isotope standard during the appropriate session are given below:

- 1: 0.511116 ± 0.11 (2SD, n = 19), blank = 2 pg
- 2: 0.511101 ± 0.09 (2SD, n = 19), blank = 3 pg.

$^{143}\text{Nd}/^{144}\text{Nd}$ are reported relative to an accepted ratio for J&M of 0.511110 (Thirlwall, 1991).

Sample	Type	Nd (ppm)	Sm (ppm)	$^{147}\text{Sm}/^{144}\text{Nd}$	$^{143}\text{Nd}/^{144}\text{Nd}$	$\varepsilon_{\text{Nd}}(t)$	F _M %	Analytical sessions
DL09-07	MME	13.1	2.76	0.1282	0.512414 (09)	-2.2	68	1
DL09-08	HR	12.7	2.88	0.1431	0.512362 (10)	-3.7	67	1
DL09-09	HR	25.7	4.16	0.0980	0.512278 (09)	-3.9	74	1
DL09-13	HR	18.1	3.25	0.1089	0.512385 (08)	-2.1	70	1
DL09-14	MME	34.6	8.25	0.1448	0.512324 (11)	-4.5	71	2
DL09-15	HR	18.0	3.60	0.1215	0.512354 (10)	-3.1	73	1
DL09-16	MME	32.4	7.57	0.1418	0.512337 (09)	-4.1	75	2
DL09-17	MME	35.2	7.94	0.1370	0.512340 (09)	-3.9	74	1
DL09-18	HR	21.1	3.64	0.1046	0.512342 (08)	-2.8	63	1
DL09-21	HR	21.7	4.22	0.1179	0.512377 (08)	-2.6	65	1
DL09-22	MME	24.9	4.87	0.1188	0.512360 (08)	-2.9	66	1
DL09-24	HR	20.0	4.42	0.1342	0.512330 (14)	-4.0	71	2
DL09-26	MME	18.7	4.60	0.1491	0.512395 (12)	-3.8	66	2
DL09-27	HR	13.4	2.50	0.1132	0.512366 (06)	-2.9	67	1
DL09-30	HR	16.0	3.14	0.0282	0.512278 (09)	-4.9	63	1
DL09-31	MME	19.5	3.91	0.0287	0.512257 (09)	-5.2	60	1
DL09-32	HR	18.7	3.73	0.0286	0.512253 (07)	-5.3	60	1

$\varepsilon_{\text{Nd}}(t) = [(\frac{^{143}\text{Nd}}{^{144}\text{Nd}})_{\text{sample}}(t) / (\frac{^{143}\text{Nd}}{^{144}\text{Nd}})_{\text{CHUR}(t)} - 1] * 10,000$, where $(\frac{^{143}\text{Nd}}{^{144}\text{Nd}})_{\text{CHUR(present)}} - (\frac{^{147}\text{Sm}}{^{144}\text{Nd}})_{\text{CHUR(present)}} * (e^{\lambda t} - 1)$, $\lambda(^{147}\text{Sm}) = 6.54 \times 10^{-12} \text{ yr}^{-1}$. The $^{147}\text{Sm}/^{144}\text{Nd}$ and $^{143}\text{Nd}/^{144}\text{Nd}$ ratios at the present day are 0.1967 and 0.512638 for chondrite, respectively. t = crystallization age of zircon, 250 Ma., F_M: mantle contribution. F_M calculation: $Nd_{\text{sample}} = Nd_{\text{mantle}} * F_M + Nd_{\text{crust}} * (1 - F_M)$, $^{143}\text{Nd}/^{144}\text{Nd}_{\text{sample}} = ^{143}\text{Nd}/^{144}\text{Nd}_{\text{Mantle}} * F_M * Nd_{\text{mantle}}/Nd_{\text{sample}} + ^{143}\text{Nd}/^{144}\text{Nd}_{\text{crust}} * (1 - F_M) * Nd_{\text{crust}}/Nd_{\text{mantle}}$.

Table 5

Whole rock Hf isotopic data. The last column refers to the analytical session during which the sample was analyzed for Hf isotope composition. The blank and average $^{176}\text{Hf}/^{177}\text{Hf}$ and reproducibility of multiple measurements of the JMC475 isotope standard during the appropriate session are given below:

- 1: 0.282148 ± 08 (2SD, n = 7), blank = 8 pg
- 2: 0.282143 ± 08 (2SD, n = 10), blank = 4 pg
- 3: 0.282146 ± 09 (2SD, n = 8), blank = 1 pg.

$^{176}\text{Hf}/^{177}\text{Hf}$ are reported relative to an accepted ratio for JMC475 of 0.282160 (Nowell et al., 1998).

Sample	Type	Lu (ppm)	Hf (ppm)	$^{176}\text{Lu}/^{177}\text{Hf}$	$^{176}\text{Hf}/^{177}\text{Hf}$ (2SD)	$\epsilon_{\text{Hf}}(t)$	F _M %	Analytical sessions
DL09-07	MME	0.29	2.89	0.014	0.282792 (14)	4.0	75	1
DL09-08	HR	0.34	4.27	0.011	0.282758 (08)	3.3	73	2
DL09-09	HR	0.32	5.39	0.008	0.282615 (11)	-1.3	62	1
DL09-13	HR	0.32	4.12	0.011	0.282735 (12)	2.5	71	1
DL09-14	MME	0.95	3.09	0.043	0.282934 (11)	4.1	75	3
DL09-15	HR	0.36	4.36	0.012	0.282766 (12)	3.5	74	1
DL09-16	MME	0.90	3.25	0.038	0.282943 (11)	5.2	77	3
DL09-17	MME	0.78	7.54	0.014	0.282805 (08)	4.4	75	1
DL09-18	HR	0.33	4.40	0.010	0.282758 (11)	3.4	73	1
DL09-21	HR	0.45	4.45	0.014	0.282759 (11)	2.8	72	1
DL09-22	MME	0.57	2.28	0.035	0.282906 (11)	4.5	76	1
DL09-24	HR	0.44	2.96	0.021	0.282764 (09)	1.8	70	1
DL09-26	MME	0.49	2.57	0.027	0.282854 (09)	4.0	75	3
DL09-27	HR	0.21	4.38	0.007	0.282709 (07)	2.3	71	2
DL09-30	HR	0.27	3.20	0.012	0.282732 (11)	2.3	71	1
DL09-31	MME	0.35	3.53	0.014	0.282595 (08)	-2.9	58	1
DL09-32	HR	0.31	3.36	0.013	0.282721 (08)	1.7	70	1

$$\epsilon_{\text{Hf}}(t) = [(\text{Lu}/^{177}\text{Hf})_{\text{sample}}(t) / (\text{Lu}/^{177}\text{Hf})_{\text{CHUR}(\text{present})} - 1] * 10,000, \text{ where } (\text{Lu}/^{177}\text{Hf})_{\text{CHUR}(\text{present})} - (\text{Lu}/^{177}\text{Hf})_{\text{CHUR}(\text{present})} * (e^{xt} - 1). \text{ The Lu}/^{177}\text{Hf} \text{ and Hf}/^{177}\text{Hf} \text{ ratios at the present day are } 0.0332 \text{ and } 0.282772 \text{ for chondrite, respectively. } t = 250 \text{ Ma. } \lambda(\text{Lu}) = 1.93 \times 10^{-11} \text{ yr}^{-1}, F_M: \text{mantle contribution. } F_M \text{ calculation: } Hf_{\text{sample}} = Hf_{\text{mantle}} * F_M + Hf_{\text{crust}} * (1 - F_M), \\ ^{176}\text{Hf}/^{177}\text{Hf}_{\text{sample}} = ^{176}\text{Hf}/^{177}\text{Hf}_{\text{Mantle}} * F_M * Hf_{\text{mantle}}/Hf_{\text{sample}} + ^{176}\text{Hf}/^{177}\text{Hf}_{\text{crust}} * (1 - F_M) * Hf_{\text{crust}}/Hf_{\text{mantle}}$$

for distinguishing mantle derived magmas (MMEs) (which should be dominated by a mantle isotopic signature) from crustal melts (granitoid hosts) (which should be dominated by a crustal isotopic signature). For example, enclaves from Crieff and Strontian plutons in northern Britain consistently have higher $\epsilon_{\text{Nd}(t)}$ than the adjacent hosts, representing the mixing process (Holden et al., 1987). Fig. 9 shows, however, that this is not the case in our study. MMEs do not have consistently higher $\epsilon_{\text{Nd}(t)}$ or $\epsilon_{\text{Hf}(t)}$ than their hosts (Fig. 10) but overlapping isotopic compositions and they do not show covariations with SiO₂ or MgO. Furthermore, even samples from the same host or the same enclave can have different initial isotopes, see ①, ②, ③ etc. in (Fig. 10). The completely overlapping initial isotopes between the host rocks and MMEs are indicative of their same origin. The initial isotopic ratio variations within individual outcrops or

enclaves largely reflect small scale isotopic heterogeneity due to incomplete homogenization of melts affected by crustal assimilation or modal variation or both. This is because granitoid magmas under sub-liquidus conditions are “crystal mashes” and complete homogenization is restricted by the efficient diffusion (Ramos and Reid, 2005; McLeod et al., 2012).

Some authors have invoked that homogenous mixing may have resulted in the overlapping Sr and Nd isotopes between MMEs and host rocks, by arguing that isotopes and trace elements diffuse faster than major elements (Mo et al., 2007b), however, this is unlikely. Indeed, elements diffuse on microscopic scales (Lesher, 1990; Allen, 1991; Holden et al., 1991), but cannot explain macroscopic process on whole magma chamber scales with the large isotopic variations within individual host rocks and MMEs. In contrast, the large variability within the individual

Table 6

Whole rock Pb isotopic data. The last column refers to the analytical session during which the sample was analyzed for Pb isotope composition. The blank and averages and reproducibility for multiple measurements of the NBS981 Pb isotope standard during the appropriate session are given below:

- 1: $^{206}\text{Pb}/^{204}\text{Pb}$: 16.94052 ± 092; $^{207}\text{Pb}/^{204}\text{Pb}$: 15.49770 ± 119; $^{208}\text{Pb}/^{204}\text{Pb}$: 36.71710 ± 382 (2SD, n = 8), blank = 10 pg
- 2: $^{206}\text{Pb}/^{204}\text{Pb}$: 16.94102 ± 184; $^{207}\text{Pb}/^{204}\text{Pb}$: 15.49811 ± 142; $^{208}\text{Pb}/^{204}\text{Pb}$: 36.71791 ± 512 (2SD, n = 11), blank = 80 pg
- 3: $^{206}\text{Pb}/^{204}\text{Pb}$: 16.94083 ± 274; $^{207}\text{Pb}/^{204}\text{Pb}$: 15.49706 ± 115; $^{208}\text{Pb}/^{204}\text{Pb}$: 36.71478 ± 399 (2SD, n = 17), blank = 79 pg.

Sample	Type	Pb (ppm)	Th (ppm)	U (ppm)	$^{206}\text{Pb}/^{204}\text{Pb}$ (2SD)	$^{207}\text{Pb}/^{204}\text{Pb}$ (2SD)	$^{208}\text{Pb}/^{204}\text{Pb}$ (2SD)	$^{208}\text{Pb}/^{204}\text{Pb}_i$	$^{207}\text{Pb}/^{204}\text{Pb}_i$	$^{206}\text{Pb}/^{204}\text{Pb}_i$	Analytical sessions
DL09-07	MME	11.5	4.1	0.7	18.634 (1)	15.642 (1)	38.752 (4)	38.475	15.634	18.480	1
DL09-08	HR	16.1	10.2	1.4	19.184 (1)	15.671 (1)	39.009 (5)	38.513	15.661	18.978	2
DL09-09	HR	14.3	11.7	1.1	18.675 (1)	15.654 (1)	39.241 (3)	38.601	15.644	18.489	1
DL09-13	HR	18.7	11.6	1.3	18.775 (1)	15.649 (1)	38.977 (3)	38.491	15.640	18.612	1
DL09-14	MME	15.5	1.7	0.6	18.658 (1)	15.642 (1)	38.574 (3)	38.487	15.637	18.561	1
DL09-15	HR	15.6	9.1	1.0	18.860 (1)	15.652 (1)	38.988 (3)	38.532	15.644	18.704	1
DL09-16	MME	12.7	2.1	0.6	18.527 (1)	15.635 (1)	38.568 (3)	38.439	15.629	18.414	2
DL09-17	MME	12.3	10.6	1.3	18.972 (1)	15.661 (1)	39.198 (4)	38.525	15.648	18.709	2
DL09-18	HR	17.2	13.8	1.1	18.645 (1)	15.645 (1)	39.130 (4)	38.502	15.638	18.496	1
DL09-21	HR	19.4	14.1	2.0	18.780 (1)	15.651 (1)	39.049 (3)	38.479	15.639	18.538	1
DL09-22	MME	10.8	3.4	0.7	18.580 (1)	15.641 (1)	38.680 (3)	38.435	15.633	18.431	1
DL09-24	HR	7.0	5.3	1.2	19.074 (1)	15.669 (1)	39.172 (4)	38.579	15.647	18.650	3
DL09-26	MME	6.5	3.8	1.3	18.968 (1)	15.665 (1)	38.996 (3)	38.533	15.641	18.503	2
DL09-27	HR	12.7	7.2	0.8	18.674 (2)	15.646 (1)	38.943 (4)	38.498	15.638	18.517	1
DL09-30	HR	9.79	6.94	0.83	18.660 (1)	15.641 (1)	38.971 (3)	36.021	15.548	16.876	2
DL09-31	MME	7.52	7.39	1.30	18.652 (1)	15.640 (1)	39.151 (5)	36.175	15.545	16.818	2
DL09-32	HR	10.4	7.25	0.98	18.610 (1)	15.638 (1)	38.963 (4)	35.990	15.543	16.786	2

$$^{206}\text{Pb}/^{204}\text{Pb}_i = (^{206}\text{Pb}/^{204}\text{Pb})_{\text{sample}} - (^{238}\text{U}/^{204}\text{Pb})_{\text{sample}} * (e^{xt} - 1) \quad t = 250 \text{ Ma. } ^{208}\text{Pb}/^{204}\text{Pb}_i \text{ and } ^{207}\text{Pb}/^{204}\text{Pb}_i \text{ are similar. } \lambda(^{238}\text{U}) = 1.55 \times 10^{-10} \text{ yr}^{-1}, \lambda(^{235}\text{U}) = 9.85 \times 10^{-10} \text{ yr}^{-1}, \\ \lambda(^{232}\text{Th}) = 4.95 \times 10^{-11} \text{ yr}^{-1}.$$

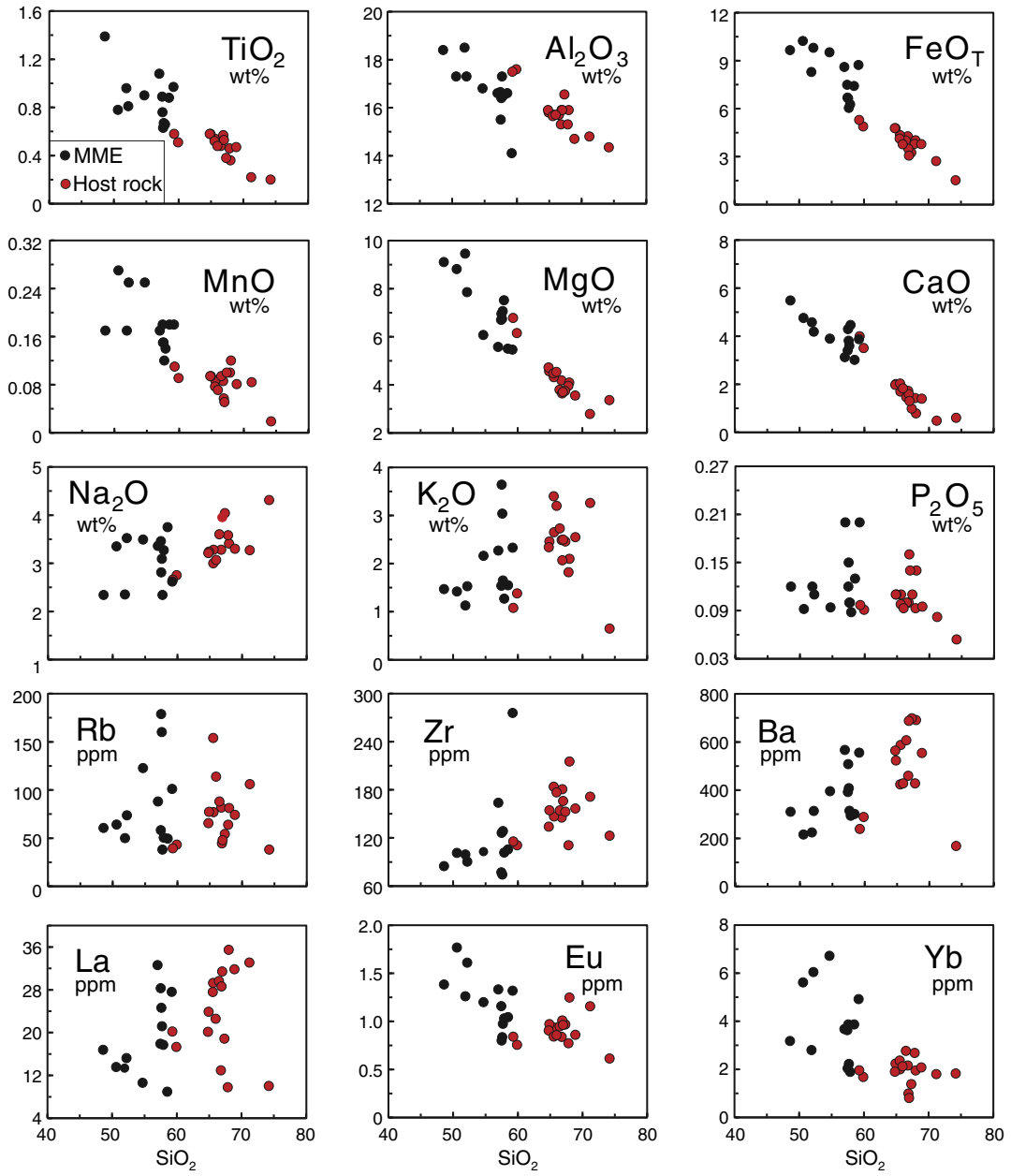


Fig. 4. SiO₂ variation diagrams of representative elements of the EKOB samples, showing fractional crystallization dominated trends.

host and MME indicates that the diffusion was rather limited. Several observations are indicative of cumulate origin for MMEs: (1) Mineralogically, the MMEs are the same as their hosts but differ in modal abundances (see Fig. 2); (2) the oval shapes and shared mineralogy imply that the MMEs were plastic and in thermal equilibrium with their hosts at the time of emplacement; (3) the coherent compositional trend on the Harker diagrams is more like liquid lines of descent (Fig. 4); (4) MMEs have higher abundances of HREEs than their respective host (Fig. S1); (5) importantly, the MMEs and host rocks have overlapping and indistinguishable isotopes (Figs. 9, 10). These all demonstrate that MMEs are disintegrated early liquidus mineral cumulate and then may have been disturbed by subsequent replenishment and induced magma convection in the magma chamber.

In this context, it is worth mentioning that some Sr–Nd–Pb isotope data reported for ‘mafic veins’ in granitoids from Yuegelu units in the EKOB have been considered as the mafic end-member during magma mixing (Liu et al., 2004b). However, these mafic veins also have the same mineralogy and same isotopes as both enclaves and hosts

granitoids (Fig. 11). We consider these ‘mafic veins’ to be large bodies of cumulate origin.

Magma mixing is a common process, and we do not intend to invalidate its role in the petrogenesis of the EK granitoids. However, our observations suggest that caution is necessary when invoking ‘magma mixing’ without a thorough consideration of the data.

5.2. Geochemical constraints on the source

Our Sr, Pb and Nd isotope data set is in agreement with previous results (Liu et al., 2004b) showing radiogenic Sr and Pb and slightly radiogenic Nd isotopes, which indicate possible contributions of continental crustal materials, whereas the notably positive $\varepsilon_{\text{HF}}(t)$ values are indicative of juvenile crustal materials and argue for significant mantle input. As the crustal contamination during melt emplacement is inevitable, the $\varepsilon_{\text{HF}}(t)$ values in the parental melt would thus have been underestimated and thus should be more positive pointing to even stronger mantle signatures. To produce large

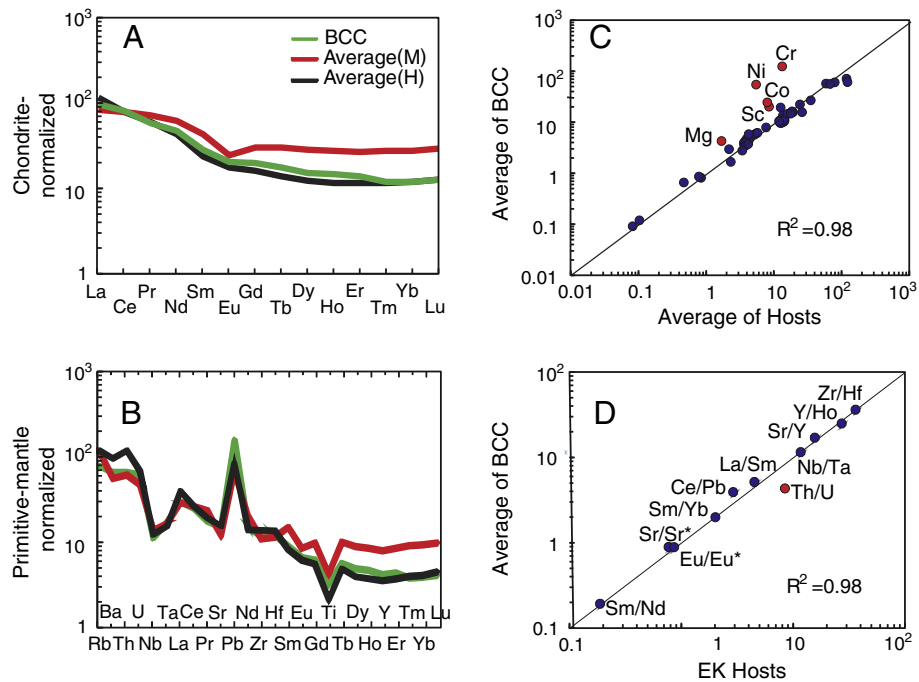


Fig. 5. A, Chondrite-normalized (Sun and McDonough, 1989) rare earth element (REE) patterns for average compositions of the EKOB granitoid hosts (H) and mafic magmatic enclaves (MME, M). Bulk continental crust (BCC; Rudnick and Gao, 2003) composition is plotted for comparison. B, Primitive mantle-normalized (Sun and McDonough, 1989) multi-element patterns as in panel A. C, One-to-one plot to show the similarity between the granitoid hosts of the EKOB samples and the BCC in terms of the analyzed major and trace elements. D, Comparison between the granitoid hosts and the BCC in terms of key elemental ratios.

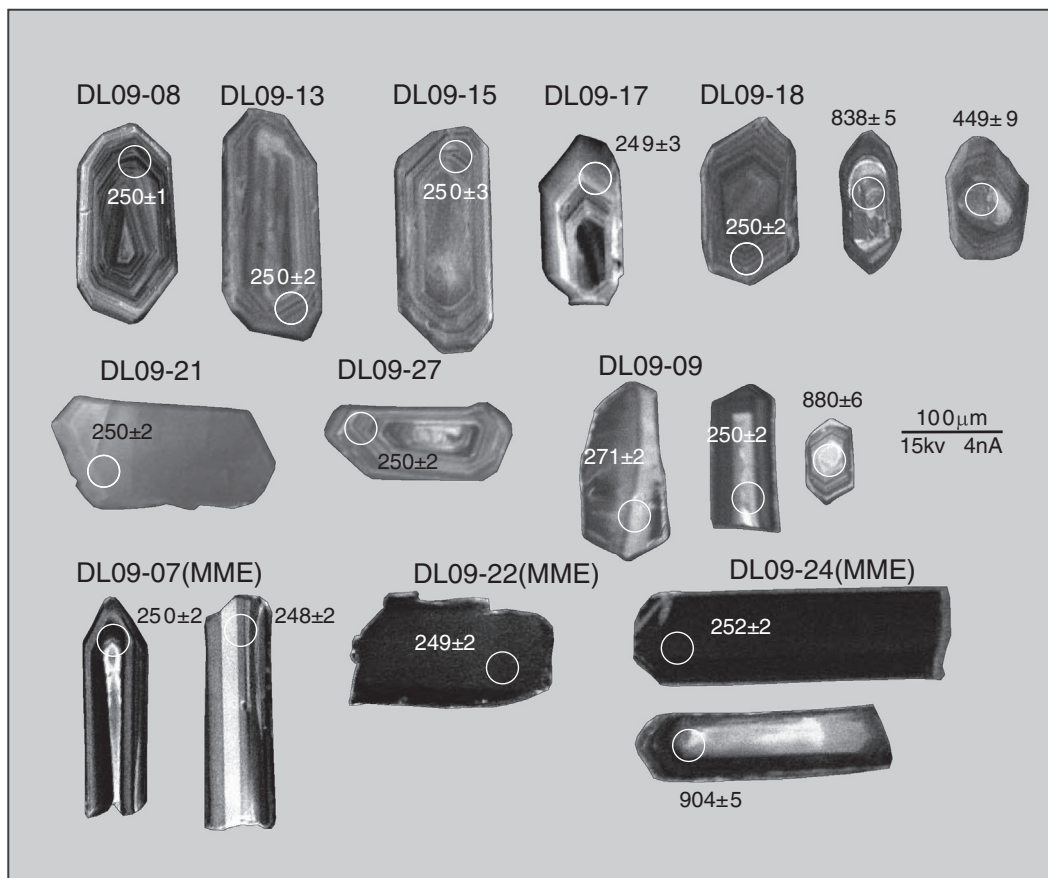


Fig. 6. Cathodoluminescence (CL) images of zircons from representative samples. White circles are the analyzed spots. The values with error are ages in Ma.

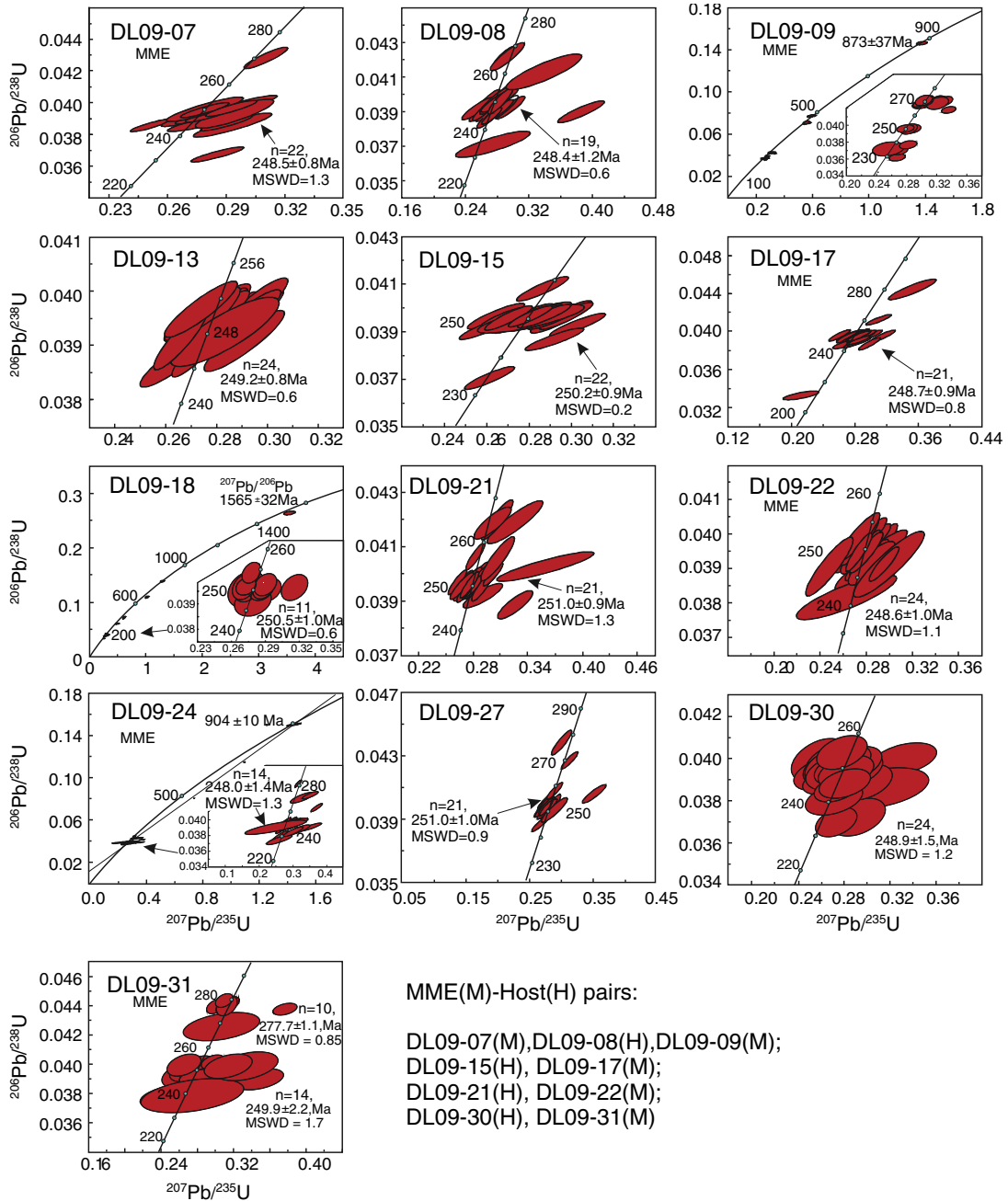


Fig. 7. Zircon U-Pb Concordia diagrams. The majority of zircons give ~250 Ma crystallization age for both granitoid hosts and the MMEs. Various amounts of inherited old zircons contained in hosts and enclaves indicate the presence and involvement of old crustal material.

volumes of andesitic batholiths with mantle isotope signature, a basaltic source is required (Mo et al., 2008). In this case, oceanic crust is the most probable candidate because it can impart its inherited mantle isotopic signatures to the derivative melt (Niu, 2005; Tatsumi, 2006; Mo et al., 2008; Niu and O'Hara, 2009). The subducted oceanic crust may be from the A'nyemagen Ocean, which is a branch of the Paleo-Tethyan that started opening around 308 Ma (Yang et al., 2009). The subducting/subducted materials comprise at least two chemically different components: altered basaltic oceanic crust and more silicic sediments (Tatsumi, 2006). The incompatible elements are depleted in the oceanic crust produced at ocean ridges but can be significantly enhanced through hydrothermal alteration and sea floor weathering especially with the involvement of terrigenous sediments of upper continental crust origin (Niu, 2005; Niu and O'Hara, 2009).

In Fig. 11, the EKOB granitoid isotope data plot along an apparent “mixing” trend between the Paleo-Tethyan oceanic crust (represented by the 350 Ma ophiolitic MORB in Qinling, central China; Xu et al., 2002) and continental crustal compositions (terrigenous sediments represented by the Shaliuhe gneiss; Meng et al., 2005a). The high $\epsilon_{\text{Hf(t)}}$ can be reasonably well modeled by melting of the Paleo-Tethyan MORB along with the subducting/subducted terrigenous sediments of Shaliuhe gneiss composition. The apparent decoupling between Nd and Hf isotopes is caused by the large difference in Nd/Hf ratios between the sediment and the oceanic crust which makes the mixing line highly curved and shift away from the terrestrial array (Fig. 11). In terms of Hf-isotopes, mass balance requires ~58–77% mantle contribution (i.e., the Paleo-Tethyan MORB), i.e., ~23–42% (Table 5) terrigenous sediments (i.e., the Shaliuhe gneiss); and requires ~60–74% mantle contribution in terms of Nd isotopes (Table 4). The Shaliuhe gneiss in the EKOB

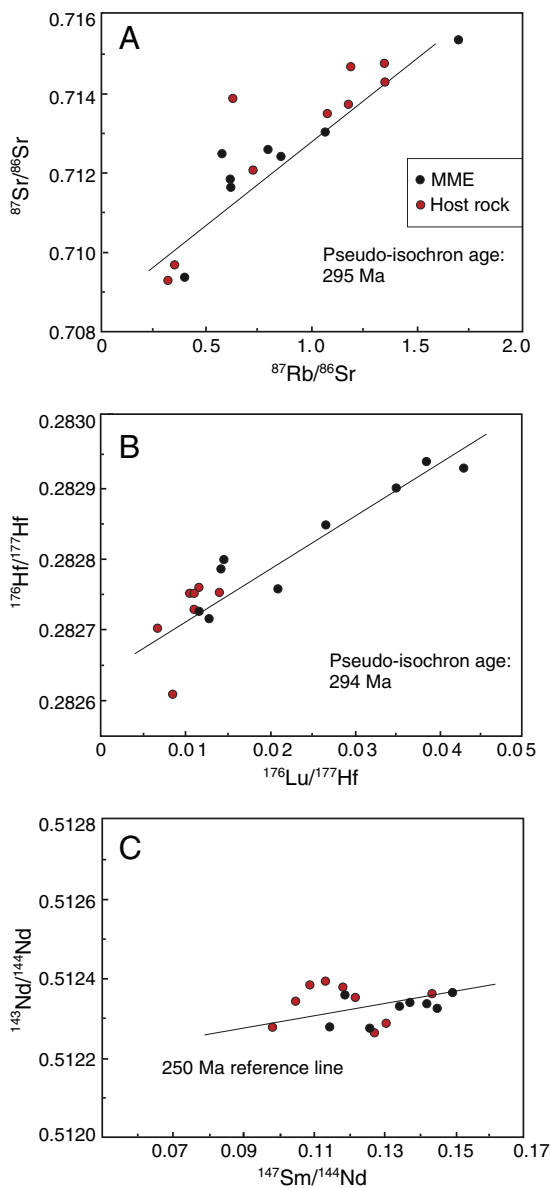


Fig. 8. A and B, Plots of isotope ratios vs. parent–daughter ratios, giving Rb/Sr pseudo-isochrone age of 295 Ma and Lu/Hf pseudo-isochron age of 294 Ma, which are close to the zircon in situ dating age of ~250 Ma of the EKOB granitoids. C, no correlation between $^{143}\text{Nd}/^{144}\text{Nd}$ and $^{147}\text{Sm}/^{144}\text{Nd}$. The 250 Ma reference line is shown to demonstrate the small ingrowth of radiogenic Nd isotopes.

dated at 920 Ma and has a metamorphic age of 400–500 Ma (Zhang et al., 2003b; Meng et al., 2005b; Chen et al., 2007a). The ~400–500 Ma granitoids are also present in the EKOB. These two time periods are consistent with the ages of inherited zircons, implying that they were both involved in the 250 Ma magmatism. Terrigenous sediments melted alongside oceanic crust also result in the isotope heterogeneity (see above) and radiogenic Sr and Pb isotopes. Despite the substantial proportion of mantle materials indicated by the isotopic compositions, the EKOB parental magmas were likely derived from partial melting of subducting oceanic crust rather than ascending asthenospheric mantle as proposed by Luo et al. (2002). The latter would produce basaltic rather than granitoid melts.

5.3. Mechanism and conditions of Paleo-Tethyan oceanic crust melting

In the pioneering studies, the trace elements for 260–240 Ma intrusions in the EKOB indicate either a post-collisional setting or an active

arc (Harris et al., 1988b). But Harris et al. (1988b) emphasized that the large long-lived magmatism required to produce such huge batholiths is more likely to occur in an active arc setting rather than a syn/post-collision setting (Harris et al., 1988b). It has been accepted since then that the period of 260–240 Ma is subduction-related. However, this interpretation did not carefully consider the stratigraphic records. The late Permian molasse (Jiang et al., 1992; Zhang et al., 2004; Li et al., 2008) indicates that the onset of collision had happened at the late Permian. Also the angular unconformity between the upper-Permian to lower-Triassic marine strata and lower-Permian terrestrial strata in the EKOB (Jiang et al., 1992; Li et al., 2008) represents a continental uplift event. Considering the strata records, the 260–240 Ma batholiths can be interpreted more precisely as syn-collisional intrusions. Furthermore, Mo et al. (2008) already demonstrated that syn-collisional magmatism is capable of producing volumetrically significant granitoid batholiths. Therefore, we argue that these granitoids were produced in a syn-collisional setting.

More and more geochemical and petrological observations have suggested that partial melting of subducted sediment/basalt is necessary (Kelemen et al., 2003 and references therein). Partial melting of subducted young, hot slab will produce high MgO andesites (Tatsumi, 2006) or ‘adakites’ (Castillo, 2006) rather than the andesitic granitoids with low MgO. Mo et al. (2008) offer a reasonable mechanism to address this issue. In their model, when the collision begins, the subducted slab evolves along a higher T/P geotherm (solid line with arrow in Fig. 12) due to the retarded underthrusting rate. This allows the slab to have longer time to approach thermal equilibrium with the prior hot active continental margin (Fig. 13B, see below) and finally melt when the highly altered oceanic crust and sediments intersect the solidus of hydrous basaltic/granitic solidi under amphibolite facies conditions (Fig. 13C). The A’nyemaqen ocean started opening in the Carboniferous (Fig. 13A, Yang et al., 2009) and closed during the late Permian (Zhang et al., 2004) before the collision between Songpan-Ganzi (SG) and Qaidam (Fig. 13B). Abundant magmatism happened during the subduction-collision time (Harris et al., 1988a) establishing a warm active continental margin environment with a geotherm of probably $> 20\text{ }^{\circ}\text{C/km}$ ($> 900\text{ }^{\circ}\text{C}$ at depths of 45 km beneath an arc; Kelemen et al., 2003) before collision (Fig. 13B). Following the simple calculation by Mo et al. (2008), we can expect at least 40,000–55,000 km³ andesitic rocks produced along the 1,000 km EKOB per Myr under the amphibolite-facies conditions (Fig. 12). It is important to note that partial melting must have taken place under the amphibolite-facies conditions because the granitoids have flat HREE patterns (Figs. 5, S1) without a ‘garnet signature’ (Mo et al., 2008; Wang et al., 2013). More evidence comes from zircon saturation temperature calculated from bulk rock compositions (Watson and Harrison, 1983) giving $\sim 734\text{ }^{\circ}\text{C}$, similar to the Amp-Pl mineral thermometer $\sim 737\text{ }^{\circ}\text{C}$ (Xiong et al., 2011). This temperature is well above the wet solidus of basaltic rocks (the wet solidus is relevant because the subducting/subducted oceanic crust must have been hydrothermally altered and weathered on the seafloor) (Mo et al., 2008).

5.4. Continental crust growth in the collision zone

Studies of the Linzizong volcanic succession (LVS) in southern Tibet have demonstrated that juvenile continental crust is produced via partial melting of the ‘trapped’ oceanic crust under the amphibolite facies conditions and preserved as ‘net crust growth’ in the collision zones (Niu et al., 2007; Mo et al., 2008; Niu and O’Hara, 2009; Niu et al., 2013). The syn-collisional Kunlun batholiths provide more geochemical and isotopic data to support this hypothesis. First of all, the bulk compositions of granitoids are similar to the bulk continental crust with almost identical sub-chondritic Nb/Ta, and Sr and Eu depletion (Fig. 5). Secondly, the whole rock Sr–Nd–Pb–Hf isotopes can be explained by partial melting of subducted Paleo-Tethyan MORB with 20%–40% terrigenous

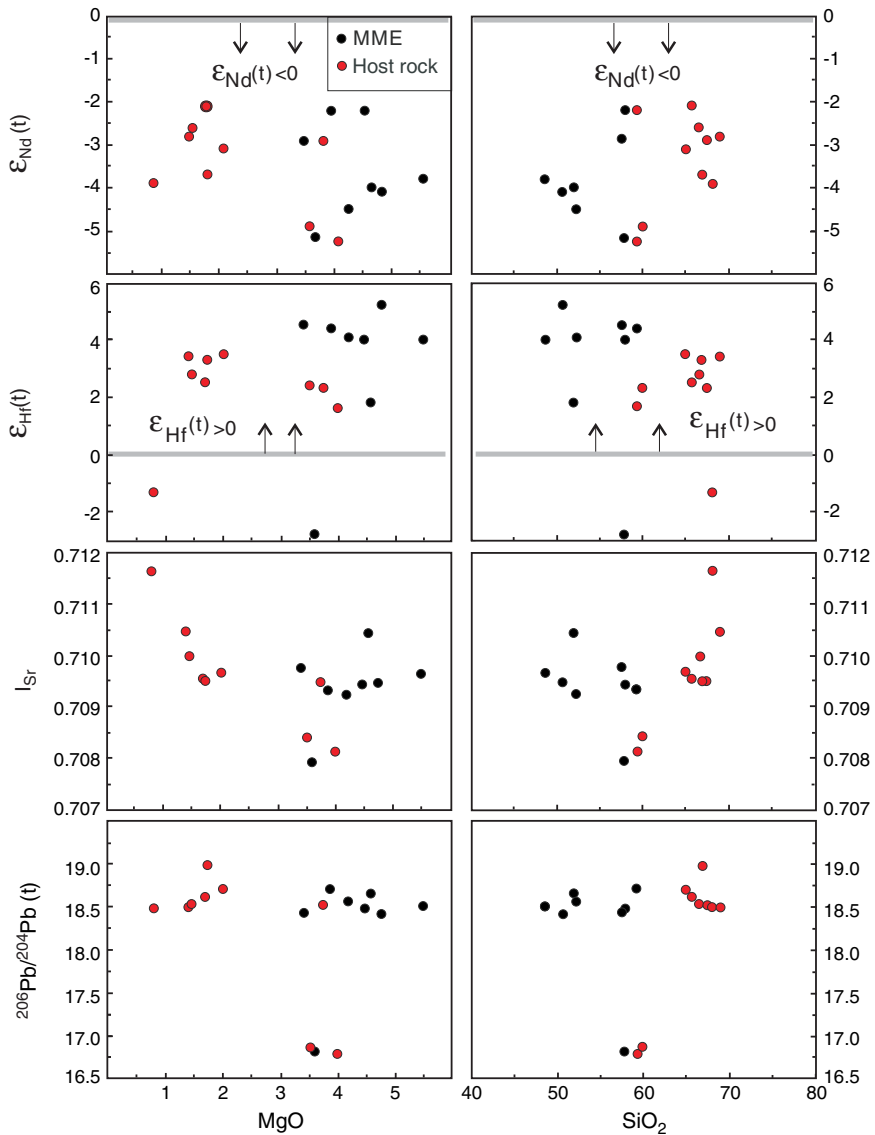


Fig. 9. Isotopes versus MgO and SiO₂ plots showing overlapping isotopes between MMEs with higher MgO/lower SiO₂ and the granitoid hosts with lower MgO/higher SiO₂. The negative $\varepsilon_{\text{Nd}}(t)$ values are suggestive of the crustal contribution while the dominant positive $\varepsilon_{\text{Hf}}(t)$ values are suggestive of mantle input.

sediments of Shaliuhe gneiss composition in the melting region under the amphibolite-facies conditions (Fig. 11). Though the granitoids in the EKOB have relatively unradiogenic Nd isotope ($\varepsilon_{\text{Nd}}(t) < 0$) compared to the LVS, they have very positive $\varepsilon_{\text{Hf}}(t)$ values (up to 5.2), which is more convincing evidence that they are juvenile crust newly formed from oceanic crust partial melting with inherited mantle isotopic signatures and crustal/sediment contribution.

6. Conclusions

1. The Permian-Triassic batholiths (240–260 Ma) along the East Kunlun Orogenic Belt (EKOB) cover an area of ~20,000 km², representing about half of all of the intrusions. They are products of syn-collisional magmatism shortly after the Late-Permian closure of the Paleo-Tethyan Ocean (A'nyemaqen branch).
2. The MMEs and granitoid hosts have the same crystallization age, share the same mineralogy and contain indistinguishable isotope compositions. Therefore, the MMEs are consistent with being cumulative lithologies of more mafic compositions produced at earlier stages of the same magmatic systems derived from partial melting

of the subducting/subducted oceanic crust. The isotope variations of similar range for both granitoid hosts and the MMEs are not the evidence of magma mixing but reflect the magma heterogeneity due to the source heterogeneity and crustal contamination on varying local scales.

3. The large volumes of these granitoids require partial melting of a basaltic source with mantle isotopic signatures. The radiogenic Sr and Pb isotopes and slightly unradiogenic Nd isotopes indicate the input of crustal materials, while the positive $\varepsilon_{\text{Hf}}(t)$ values emphasize the significant mantle contribution. Although $\varepsilon_{\text{Hf}}(t)$ is elevated at a given $\varepsilon_{\text{Nd}}(t)$, it can be readily explained by partial melting of the subducted Paleo-Tethyan MORB alongside the terrestrial sediments represented by Shaliuhe gneiss under the amphibolite-facies condition. Both Nd and Hf isotopic modelings indicate ~60–80% mantle input.
4. The granitoids have broad compositional similarities to the bulk continental crust and have a large mantle component, thus representing newly formed juvenile crustal contributions in the EKOB. Although the closure time of the Paleo-Tethyan ocean is not well constrained, the stratigraphic records (the late-Permian molasses, the

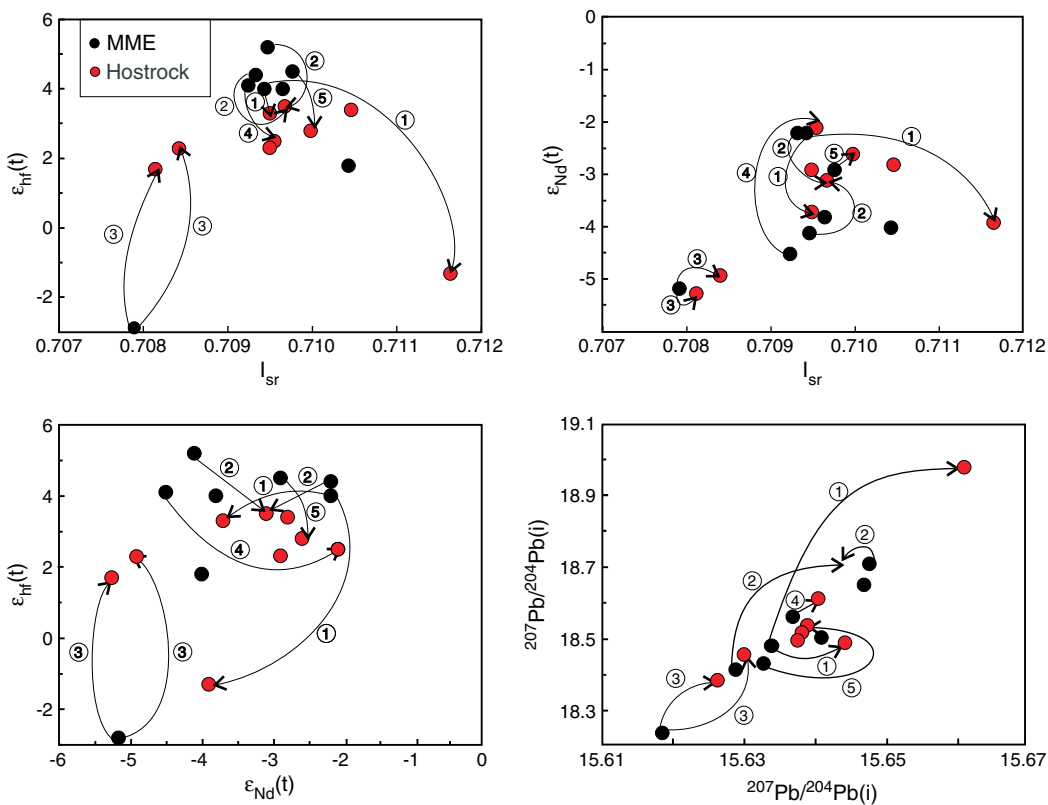


Fig. 10. Small scale age-corrected (250 Ma) isotope variation diagrams showing overlapping isotopes between the granitoid hosts and MMEs and isotopic variations within individual host and MME, which actually reflect magma heterogeneity (with some superimposed mineralogical differences) rather than mixing process. MME(M)–Host(H) pairs: ①: DL09-07(M), DL09-08(H), DL09-09(H) (two host rocks for the same MME); ②: DL09-15(H), DL09-16(M), DL09-17(M) (two enclaves for the same host rock); ③: DL09-30(H), DL09-31(M), DL09-32(H) (two host rocks for the same enclaves). Others, ④: DL09-13(H), DL09-14(M); ⑤: DL09-21(H), DL09-22(M). H: host rock; M: MME.

unconformity between upper-Permian to lower-Triassic and lower Permian sequences) indicate that the onset of collision was during the late Permian. Therefore, these granitoids were formed in a syn-collisional setting, and offer new evidence in support of the hypothesis that collision zones are primary sites where net continental crust is produced and preserved.

Acknowledgment

We thank Yongshan Bai for assistance in the field, Lei Wu and Xiaoli Xu for help with major and trace element analysis; Chris Dale and Scott Dempsey for help in the Sr–Nd–Pb–Hf isotope analysis. Discussion with Mark Allen, Iain Neil and Shuijiong Wang was useful. Thanks to Helen Foster for the comments on the early manuscript. Thanks to two anonymous reviewers whose comments and suggestions have helped improve this paper significantly. Further thanks are owed to the Editor Laurie Reisberg who provided very detailed and constructive comments and suggestions. The research was supported by National Natural Science Foundation of China (NSFC: 91014003, 41130314, 41273044, 41225006) and other Chinese funding agencies (Qianren Plan Funds; Project 973: 2011CB403102, Sinoprobe-04-02, IRT1083; Program 111: B07011). Hui is supported by Durham University Doctoral scholarship and China Scholarship Council.

Appendix A. Supplementary data

Supplementary data to this article can be found online at <http://dx.doi.org/10.1016/j.chemgeo.2014.01.010>.

References

- Allen, C.M., 1991. Local equilibrium of mafic enclaves and granitoids of the turtle pluton, southeast California: Mineral, chemical, and isotopic evidence. *Am. Mineral.* 76, 574–588.
- Andersen, T., 2002. Correction of common lead in U–Pb analyses that do not report ^{204}Pb . *Chem. Geol.* 192, 59–79.
- Arculus, R.J., 1981. Island arc magmatism in relation to the evolution of the crust and mantle. *Tectonophysics* 75, 113–133.
- Barbarin, B., 2005. Mafic magmatic enclaves and mafic rocks associated with some granitoids of the central Sierra Nevada batholith, California: nature, origin, and relations with the hosts. *Lithos* 80, 155–177.
- Bizimis, M., Sen, G., Salters, V.J.M., 2004. Hf–Nd isotope decoupling in the oceanic lithosphere: constraints from spinel peridotites from Oahu, Hawaii. *Earth Planet. Sci. Lett.* 217, 43–58.
- Castillo, P.R., 2006. An overview of adakite petrogenesis. *Chin. Sci. Bull.* 51, 257–268.
- Chappell, B.W., White, A.J.R., Wyborn, D., 1987. The importance of residual source material (restite) in granite petrogenesis. *J. Petrol.* 28, 1111–1138.
- Chappell, B.W., White, A.J.R., Williams, I.S., Wyborn, D., Herdt, J.M., Woodhead, J.D., 1999. Evaluation of petrogenetic models for lachlan fold belt granitoids: Implications for crustal architecture and tectonic models – discussion. *Aust. J. Earth Sci.* 46, 827–831.
- Chauvel, C., Lewin, E., Carpentier, M., Arndt, N.T., Marini, J.C., 2008. Role of recycled oceanic basalt and sediment in generating the Hf–Nd mantle array. *Nat. Geosci.* 1, 64–67.
- Chen, H.W., Luo, Z.H., Mo, X.X., Liu, C., Ke, S., 2005. Underplating mechanism of triassic granite of magma mixing origin in the east Kunlun orogenic belt. *Geol. China* 32, 386–393 (in Chinese with English abstract).
- Chen, N.S., Wang, X.Y., Zhang, H.F., 2007a. Components and metamorphism of the base-metamorphic rocks of the Qaidam and Oulongbuluke micro-continental blocks, and a tentative interpretation of paleocontinental evolution in NW-Central China. *Earth Sci. Front.* 14, 43.
- Chen, N.S., Wang, X.Y., Zhang, H.F., Sun, M., Li, X.Y., Chen, Q., 2007b. Geochemistry and Nd–Sr–Pb isotopic compositions of granitoids from Qaidam and Oulongbuluke micro-blocks, NW China constraints on basement nature and tectonic affinity. *J. Earth Sci.* 32, 7–21 (in Chinese with English Abstract).
- Chen, N.S., Xia, X.P., Li, X.Y., Sun, M., 2007c. Timing of magmatism of the gneissic–granite plutons along north Qaidam margin and implications for Precambrian crustal accretions: Zircon U–Pb dating and Hf isotope evidences. *Acta Petrol. Sin.* 23, 501–512 (in Chinese with English abstract).

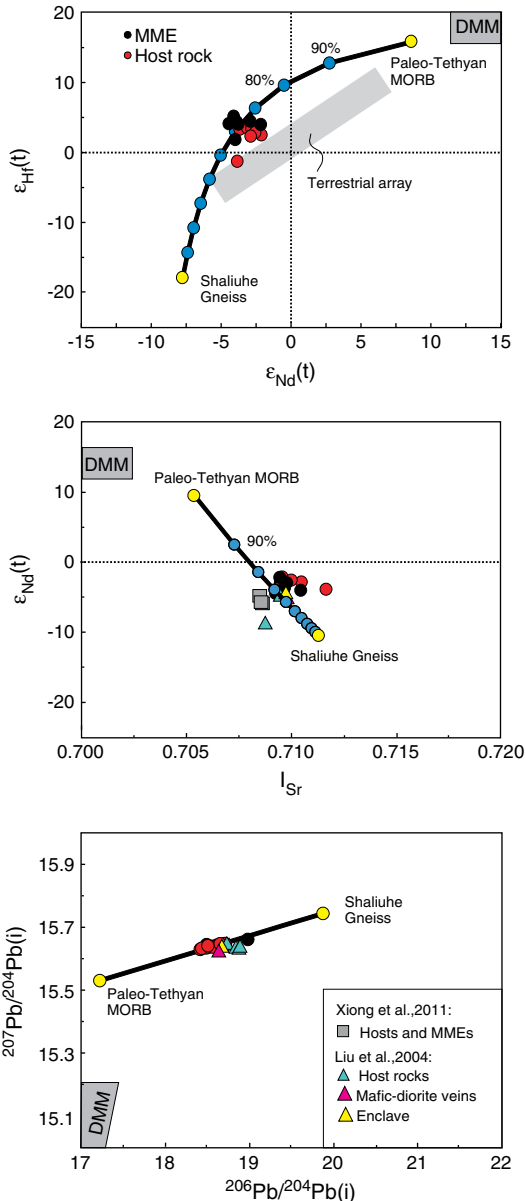


Fig. 11. Showing that the mafic enclaves (MME), host rocks in this study and mafic-diorite veins in the literature (Liu et al., 2004b; Xiong et al., 2011) all have indistinguishable isotope compositions and they plot along an apparent ‘mixing’ trend between Paleo-Tethyan MORB and terrestrial sediments (the Shaliuhe gneiss). Terrestrial array is from Chauvel et al. (2008). Sr, Nd and Pb isotopes and elemental concentrations for Paleo-Tethyan MORB are from the east part of the northernmost branch of the Paleo-Tethyan realm ($^{87}\text{Sr}/^{86}\text{Sr}$: 0.7055, $^{143}\text{Nd}/^{144}\text{Nd}$: 0.51313, $^{206}\text{Pb}/^{204}\text{Pb}$: 17.257, $^{207}\text{Pb}/^{204}\text{Pb}$: 15.532, Sr: 69.07 ppm, Nd: 6.5 ppm, Hf: 1.87 ppm, Pb: 1.91 ppm) (Xu et al., 2002). Hf isotope for MORB is inferred from Nd isotope following the equation ($\epsilon_{\text{Hf}} = 1.59_{\text{Nd}} + 1.28$) given by Chauvel et al. (2008) because of the statistically significant Hf-Nd isotope ratio correlation (Zindler and Hart, 1986). Sr isotope ($^{87}\text{Sr}/^{86}\text{Sr}$: 0.7180, Sr: 300 ppm) for the Shaliuhe Gneiss is from Harris et al. (1988a). Nd and Pb isotope data ($^{143}\text{Nd}/^{144}\text{Nd}$: 0.5121, $^{206}\text{Pb}/^{204}\text{Pb}$: 20.000, $^{207}\text{Pb}/^{204}\text{Pb}$: 15.750, Nd: 33 ppm, Pb: 19.50 ppm) for the Shaliuhe Gneiss are from Chen et al. (2007b) and Meng et al. (2005a). Hf isotope data ($^{176}\text{Hf}/^{177}\text{Hf}$: 0.28218, Hf: 4 ppm) for the Shaliuhe Gneiss are from Chen et al. (2007c). Gray square: Host rocks and enclaves from (Xiong et al., 2011). Triangle: host rocks, enclaves and mafic veins from Liu et al. (2004b).

- Chen, X.H., Yin, A., George, G., Li, L., Jiang, R.B., 2011. Chemical geodynamics of granitic magmatism in the basement of the eastern Qaidam basin, northern Qinghai-Tibet Plateau. *Acta Geol. Sin.* 85, 157–171 (in Chinese).
- Clemens, J.D., Stevens, G., 2011. What controls chemical variation in granitic magmas. *Lithos* 134–135, 317–329.
- Clift, P.D., Vannucchi, P., 2004. Controls on tectonic accretion versus erosion in subduction zones: implications for the origin and recycling of the continental crust. *Rev. Geophys.* 42, 31.

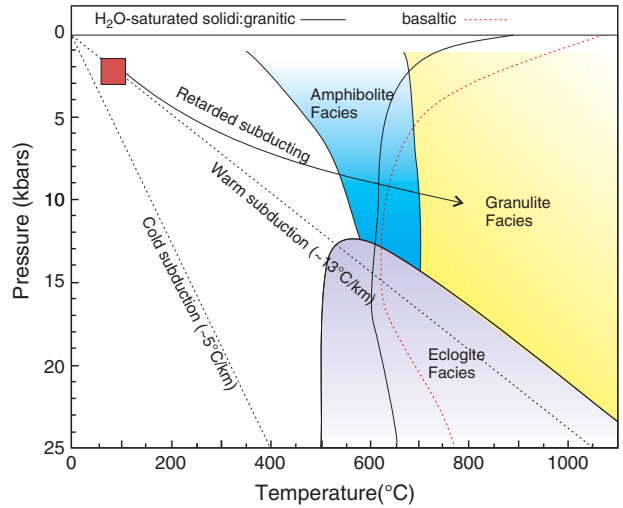


Fig. 12. Simplified phase diagram showing hydrous solidi of basalts and granitic rocks quoted from Mo et al. (2008) (after Niu, 2005). The solid line with arrow illustrates the concept of the subducted oceanic crust (A’nyemaqen Ocean) evolve along a high T/P path as a result of retarded subducting and enhanced heating upon continental collision at a prior active continental margin setting.

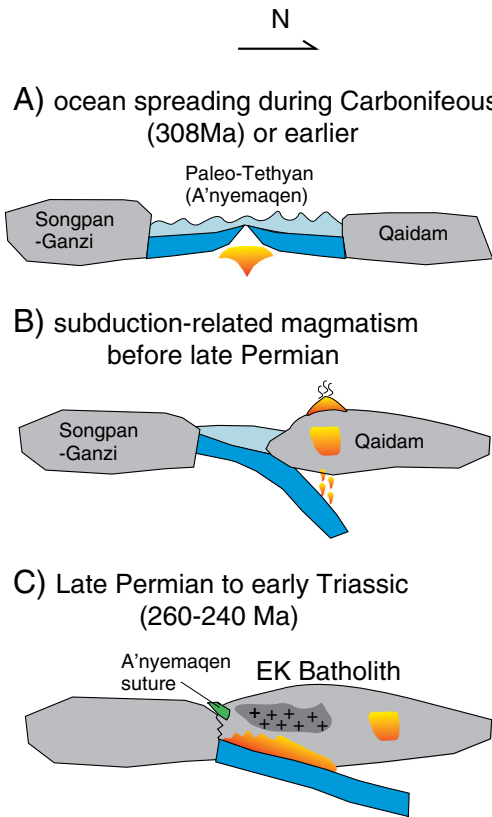


Fig. 13. Cartoons showing the A’nyemaqen seafloor spreading during the Carboniferous time (A) (308 Ma: the protolith age of Dur’ngoi ophiolite (Yang et al., 2009)), subduction of A’nyemaqen oceanic crust and related magmatism (B) and the synollisional magmatism (C; see Fig. 12 for mechanisms).

- Clift, P.D., Schouten, H., Vannucchi, P., 2009. Arc-continent collisions, sediment recycling and the maintenance of the continental crust. *Geol. Soc. Lond. Spec. Publ.* 318, 75–103.
- Condie, K.C., 2000. Episodic continental growth models: afterthoughts and extensions. *Tectonophysics* 322, 153–162.
- Dahlquist, J., 2002. Mafic microgranular enclaves: early segregation from metaluminous magma (sierra de chepes), pampean ranges, NW Argentina. *J. S. Am. Earth Sci.* 15, 643–655.
- Deng, J., Luo, Z.H., Su, S.G., 2004. Petrogenesis, Tectonic Setting and Mineralization. *Geol. Pub. House, Beijing* 1–381 (in Chinese).

- Dewey, J.F., Shackleton, R.M., Cheng, C.F., Sun, Y.Y., 1988. The tectonic evolution of the Tibetan Plateau. *Philos. Trans. R. Soc. A Math. Phys. Eng. Sci.* 327 (1594), 379–413.
- Foley, S.F., Barth, M.G., Jenner, G.A., 2000. Rutile/melt partition coefficients for trace elements and an assessment of the influence of rutile on the trace element characteristics of subduction zone magmas. *Geochim. Cosmochim. Acta* 64, 933–938.
- Fujimaki, H., 1986. Partition-coefficients of Hf, Zr, and REE between zircon, apatite, and liquid. *Contrib. Mineral. Petrol.* 94 (1), 42–45.
- Gill, J.B., 1981. Orogenic Andesites and Plate Tectonics, 16. Springer-Verlag, New York, p. 390.
- Hans Wedepohl, K., 1995. The composition of the continental crust. *Geochim. Cosmochim. Acta* 59, 1217–1232.
- Harris, N.B.W., Hua, X.R., Lewis, C.L., Hawkesworth, C.J., Zhang, Y.Q., 1988a. Isotope geochemistry of the 1985 Tibet geotraverse, Lhasa to Golmud. The geological evolution of Tibet. *Philosophical Transactions of the Royal Society of London*, 327, pp. 263–285.
- Harris, N.B.W., Xu, R.H., Lewis, C.L., Jin, C., 1988b. Plutonic rocks of the 1985 Tibet geotraverse, Lhasa to Golmud. *Philos. Trans. R. Soc. Lond.* 327, 145–168.
- Hoffmann, J.E., Münker, C., Polat, A., Rosing, M.T., Schulz, T., 2011. The origin of decoupled Hf–Nd isotope compositions in Eoarchean rocks from southern west Greenland. *Geochim. Cosmochim. Acta* 75, 6610–6628.
- Holden, P., Halliday, A.N., Stephens, W.E., 1987. Neodymium and strontium isotope content of microdiorite enclaves points to mantle input to granitoid production. *Nature* 330, 53–55.
- Holden, P., Halliday, A.N., Stephens, W., Henney, P.J., 1991. Chemical and isotopic evidence for major mass transfer between mafic enclaves and felsic magma. *Chem. Geol.* 92, 135–152.
- Irvine, T.N., Baragar, W.R.A., 1971. A guide to the chemical classification of the common volcanic rocks. *Can. J. Earth Sci.* 8, 523–548.
- Jiang, C.F., Yang, J.S., Feng, B.G., 1992. Opening–closing evolution of the Kunlun mountains. In: Jiang, C.F., Yang, J.S., Feng, B.G. (Eds.), *Opening Closing Tectonics of Kunlun Mountain*. Geological Publishing House, Beijing, pp. 205–271 (in Chinese).
- Kelemen, P.B., Rilling, J.L., Parmentier, E., Mehl, L., Hacker, B.R., 2003. Thermal structure due to solid-state flow in the mantle wedge beneath arcs. *Geophys. Monogr. Am. Geophys. Union* 138, 293–311.
- Lesher, C.E., 1990. Decoupling of chemical and isotopic exchange during magma mixing. *Nature* 344, 235–237.
- Li, R.S., Xu, W.H., Yang, Y.C., 2008. *Kunlun Mountains and Geology of Adjacent Areas*. Geological Publishing House, Beijing (in Chinese with English abstract).
- Li, X.L., Chen, X., Ge, H.J., Wu, Y.T., Xian, X.L., Han, W., 2011. XRF determination of chlorine etc multi-elements in sea sediments with sample preparation by fusion. *Phys. Test. Chem. Anal. B Chem. Anal.* 47, 1420–1423 (in Chinese with English abstract).
- Liu, C.D., Mo, X.X., Luo, Z.H., Yu, X.H., 2004a. Mixing events between the crust and mantle derived magmas in eastern Kunlun: evidence from zircon SHRIMP chronology. *Chin. Sci. Bull.* 49, 828–834 (in Chinese).
- Liu, C.D., Mo, X.X., Luo, Z.H., Yu, X.H., 2004b. Pb–Sr–Nd–O isotope characteristics of granitoids in east Kunlun orogenic belt. *J. Earth Sci.* 24 (6), 584–588 (in Chinese with English abstract).
- Liu, Y.S., Hu, Z.C., Gao, S., Gunther, D., Xu, J., Gao, C.G., Chen, H.H., 2008. In situ analysis of major and trace elements of anhydrous minerals by LA-ICP-MS without applying an internal standard. *Chem. Geol.* 257, 34–43.
- Ludwig, K.R., 2003. A geochronological toolkit for microsoft excel. *Isoplot* 3, 1–70.
- Luo, Z.H., Ke, S., Cao, Y.Q., Deng, J.F., Chen, H.W., 2002. Late Indosinian mantle-derived magmatism in the east Kunlun. *Geol. Bull. China* 21 (6), 292–297 (in Chinese with English abstract).
- McLeod, C.L., Davidson, J.P., Nowell, G.F., Silva, S.I., 2012. Disequilibrium melting during crustal anatexis and implications for modelling open magmatic systems. *Geology* 40, 435–438.
- Meng, F.C., Zhang, J.X., Yang, J.S., 2005a. Subducted continental arc: geochemical and isotope evidence of gneisses in the north Qaidam. *Acta Petro. Sin.* 79, 46–55 (in Chinese with English abstract).
- Meng, F.C., Zhang, J.X., Yang, J.S., 2005b. Tectono-thermal event of post-HP/UHP metamorphism in the Xiteshan area of the north Qaidam mountain, west China: isotope and geochemical evidence of granite and gneiss. *Acta Petro. Sin.* 21, 45–56 (in Chinese with English abstract).
- Mo, X.X., Hou, Z.Q., Niu, Y.L., Dong, G.C., Qu, X.M., Zhao, Z.D., Yang, Z.M., 2007a. Mantle contributions to crustal thickening during continental collision: evidence from Cenozoic igneous rocks in southern Tibet. *Lithos* 96, 225–242.
- Mo, X.X., Luo, Z.H., Deng, J.F., Yu, X.H., 2007b. Granitoids and crustal growth in the east-Kunlun orogenic belt. *Geol. J. China Univ.* 3, 403–414 (in Chinese with English abstract).
- Mo, X.X., Niu, Y.L., Dong, G.C., Zhao, Z.D., Hou, Z.Q., Zhou, S., Ke, S., 2008. Contribution of collisional felsic magmatism to continental crust growth: a case study of the Paleogene Linzizong volcanic succession in southern Tibet. *Chem. Geol.* 250, 49–67.
- Niu, Y.L., 2005. Generation and evolution of basaltic magmas: Some basic concepts and a new view on the origin of Mesozoic–Cenozoic basaltic volcanism in eastern China. *Geol. J. China Univ.* 11, 9–46.
- Niu, Y.L., O'Hara, M.J., 2009. MORB mantle hosts the missing Eu (Sr, Nb, Ta and Ti) in the continental crust: new perspectives on crustal growth, crust–mantle differentiation and chemical structure of oceanic upper mantle. *Lithos* 112, 1–17.
- Niu, Y.L., Mo, X.X., Dong, G.C., Zhao, Z.D., Hou, Z.Q., Zhou, S., Ke, S., 2007. Continental collision zones are primary sites of net continental crustal growth: evidence from the Linzizong volcanic succession in southern Tibet. *EOS Trans. Am. Geophys. Union* 88 (52), 01 (Fall meet, Suppl., Abstract).
- Niu, Y.L., Zhao, Z.D., Zhu, D.C., Mo, X.X., 2013. Continental collision zones are primary sites for net continental crust growth – a testable hypothesis. *Earth-Sci. Rev.* 127, 96–110.
- Nowell, G.M., Parrish, R.R., 2001. Simultaneous acquisition of isotope compositions and parent/daughter ratios by non-isotope dilution solution-mode plasma ionisation multi-collector mass spectrometry (PIMMS). *Plasma Source Mass Spectrometry: the new millennium. R. Soc. Chem. Spec. Publ.* 267, 298–310.
- Nowell, G.M., Kempton, P.D., Noble, S.R., Fitton, J.G., Saunders, A.D., Mahoney, J.J., Taylor, R.N., 1998. High precision Hf isotope measurements of MORB and OIB by thermal ionisation mass spectrometry: insights into the depleted mantle. *Chem. Geol.* 149, 211–233.
- Nowell, G.M., Pearson, D.G., Ottley, C.J., Schweiters, J., Dowall, D., 2003. Long-term performance characteristics of a plasma ionisation multi-collector mass spectrometer (PIMMS): the thermofinnigan neptune. *Plasma Source Mass Spectrometry: Applications and Emerging Technologies*Royal Society of Chemistry, Cambridge 307–320.
- Pan, G.T., Ding, J., Yao, D.S.W., L. Q., 2004. *Geological Map of the Qinghai-Xizang (Tibet) Plateau and Adjacent Areas*. Chengdu Cartographic Publishing House.
- Pearcy, L.G., DeBari, S.M., Sleep, N.H., 1990. Mass balance calculations for two sections of island arc crust and implications for the formation of continents. *Earth Planet. Sci. Lett.* 96, 427–442.
- Ramos, F.C., Reid, M.R., 2005. Distinguishing melting of heterogeneous mantle sources from crustal contamination: insights from Sr isotopes at the Phenocryst Scale, Pisgah Crater, California. *J. Petrol.* 46, 999–1012.
- Reymer, A., Schubert, G., 1984. Phanerozoic addition rates to the continental crust and crustal growth. *Tectonics* 3, 63–77.
- Rudnick, R.L., Gao, S., 2003. Composition of the continental crust. *Treatise Geochem.* 1–64.
- Schmitz, M.D., Vervoort, J.D., Bowring, S.A., Patchett, P.J., 2004. Decoupling of the Lu–Hf and Sm–Nd isotope systems during the evolution of granulitic lower crust beneath southern Africa. *Geology* 32 (5), 405.
- Scholl, D.W., von Huene, R., 2009. Implications of estimated magmatic additions and recycling losses at the subduction zones of accretionary (non-collisional) and collisional (suturing) orogens. *Geol. Soc. Lond. Spec. Publ.* 318, 105–125.
- Sun, S.-S., McDonough, W.F., 1989. Chemical and isotopic systematics of oceanic basalts: implications for mantle composition and processes. *Geological Society, London, Special Publications* 42, 313–345.
- Sun, Y., Pei, X.Z., Ding, S.P., Li, R.B., Feng, J.B., Zhang, Y.F., 2009. Halagatu magma mixing granite in the east kunlun mountains—evidence from zircon U–Pb dating. *Acta Petro. Sin.* 83, 1000–1010 (in Chinese with English abstract).
- Tatsumi, Y., 2006. High-Mg andesites in the Setouchi volcanic belt, southwestern Japan: analogy to Archean magmatism and continental crust formation? *Annu. Rev. Earth Planet. Sci.* 34, 467–499.
- Taylor, S.R., 1967. The origin and growth of continents. *Tectonophysics* 4, 17–34.
- Taylor, S.R., 1977. Island arc models and the composition of the continental crust. *Island Arcs, Deep-Sea Trenches and Back-Arc Basins*American Geophysical Union, Washington, DC 325–335.
- Taylor, S.R., McLennan, S.M., 1985. *The Continental Crust: Its Composition and Evolution*. Blackwell Scientific Pub., Palo Alto, CA.
- Thirlwall, M.F., 1991. Long-term reproducibility of multicollector Sr and Nd isotope ratio analysis. *Chem. Geol. Isot. Geosci.* 94, 85–104.
- von Huene, R., Scholl, D.W., 1991. Observations at convergent margins concerning sediment subduction, subduction erosion, and the growth of continental crust. *Rev. Geophys.* 29, 279–316.
- Wall, V.J., Clemens, J.D., Clarke, D.B., 1987. Models for granitoid evolution and source compositions. *J. Geol.* 95, 731–749.
- Wang, S.J., Li, S.G., Chen, L.J., He, Y.S., An, S.C., Shen, J., 2013. Geochronology and geochemistry of leucosomes in the North Dabie Terrane, East China: implication for post-UHPM crustal melting during exhumation. *Contrib. Mineral. Petrol.* 165, 1009–1029.
- Watson, E.B., Harrison, T.M., 1983. Zircon saturation revisited: temperature and composition effects in a variety of crustal magma types. *Earth Planet. Sci. Lett.* 64, 295–304.
- Winter, J.D., 2010. *An Introduction to Igneous and Metamorphic Petrology*, Second edition. Prentice Hall, London.
- Xiong, F.H., Ma, C.Q., Zhang, J.Y., Liu, B., 2011. The origin of mafic microgranular enclaves and their host granodiorites from east Kunlun, northern Qinghai–Tibet Plateau: implications for magma mixing during subduction of Paleo-Tethyan lithosphere. *Mineral. Petrol.* 104, 1–14.
- Xu, J.F., Castillo, P.R., Li, X.H., Zhang, B.R., Han, Y.W., 2002. MORB-type rocks from the Paleo-Tethyan mian-lueyang northern ophiolite in the Qinling mountains, central china: implications for the source of the low $^{206}\text{Pb}/^{204}\text{Pb}$ and high $^{143}\text{Nd}/^{144}\text{Nd}$ mantle component in the Indian ocean. *Earth Planet. Sci. Lett.* 198, 323–337.
- Yang, J.S., Qu, J.C., Xu, Z.Q., 1995. Qingshuiquan ophiolite of east Kunlun: a lower Paleozoic suture. *Abstract for the Symposium of Uplift Deformation and Deep Structure of Northern Tibet. 1995 September. Montpellier, France (Abstract No.48)*.
- Yang, J.S., Robinson, P.T., Jiang, C.F., Xu, Z.Q., 1996. Ophiolites of the Kunlun mountains, China and their tectonic implications. *Tectonophysics* 258, 215–231.
- Yang, J.S., Xu, Z.Q., Li, H.B., Shi, R.D., 2005. The Paleo-Tethyan volcanism and plate tectonic regime in the A'nyemaqen region of east Kunlun, northern Tibet Plateau. *Acta Petro. Mineral.* 24, 369–380 (in Chinese with English abstract).
- Yang, J.S., Wu, F.Y., Wilde, S., Liu, X., 2007. Petrogenesis of late Triassic granitoids and their enclaves with implications for post-collisional lithospheric thinning of the Liaodong Peninsula, North China Craton. *Chem. Geol.* 242, 155–175.
- Yang, J.S., Shi, R.D., Wu, C.L., Wang, X.B., Robinson, P.T., 2009. Dur'ngoi ophiolite in east Kunlun, northeast Tibetan Plateau: Evidence for Paleo-Tethyan suture in northwest China. *J. Earth Sci.* 20, 303–331.
- Yin, A., Harrison, T.M., 2000. Geologic evolution of the Himalayan–Tibetan orogen. *Annu. Rev. Earth Planet. Sci.* 28, 211–280.
- Yin, H.F., Zhang, K.X., 1997. Characteristics of the eastern Kunlun orogenic belt. *Earth Sci. J. China Univ. Geosc.* 22, 339–342.

- Zhang, J.X., Meng, F.C., Wan, Y.S., Yang, J.S., Tung, K.A., 2003a. Early Paleozoic Tectono-thermal event of the Jingshuikou group on the south margin of Qaidam: zircon U-Pb SHRIMP age evidence. *Geol. Bull. China* 22, 397–404 (in Chinese with English abstract).
- Zhang, J.X., Wan, Y.S., Meng, F.C., Yang, J.S., Xu, Z.Q., 2003b. Geochemistry, Sm-Nd and U-Pb isotope study of gneisses (schists) enclosing eclogites in the north Qaidam mountains – deeply subducted Precambrian metamorphic basement. *Acta Petrol. Sin.* 19, 443–451 (in Chinese with English abstract).
- Zhang, K.X., Zhu, Y.H., Yin, H.F., 2004. Application of tectonic facies in geological mapping in east Kunlun orogenic belt. *Earth Sci. J. China Univ. Geosci.* 29, 661–666 (in Chinese with English abstract).
- Zindler, A., Hart, S., 1986. Chemical geodynamics. *Earth Planet. Sci. Lett.* 14, 493–571.